



# Assessing spectra and thermal inversions due to TiO in hot Jupiter atmospheres

Anjali A. A. Piette<sup>1,2</sup>, Nikku Madhusudhan<sup>1,3</sup>, Laura K. McKemmish,<sup>2</sup> Siddharth Gandhi<sup>1,3</sup>, Thomas Masseron<sup>4,5</sup> and Luis Welbanks<sup>1</sup>

<sup>1</sup>Institute of Astronomy, University of Cambridge, Madingley Road, Cambridge CB3 0HA, UK

<sup>2</sup>School of Chemistry, University of New South Wales, Kensington, Sydney 2052, Australia

<sup>3</sup>Department of Physics, University of Warwick, Gibbet Hill Road, Coventry CV4 7AL, UK

<sup>4</sup>Instituto de Astrofísica de Canarias, E-38205 La Laguna, Tenerife, Spain

<sup>5</sup>Departamento de Astrofísica, Universidad de La Laguna, E-38206 La Laguna, Tenerife, Spain

Accepted 2020 June 3. Received 2020 June 3; in original form 2019 August 1

## ABSTRACT

Recent detections of thermal inversions in the dayside atmospheres of some hot Jupiters are motivating new avenues to understand the interplay between their temperature structures and other atmospheric conditions. In particular, TiO has long been proposed to cause thermal inversions in hot Jupiters, depending on other factors such as stellar irradiation, C/O, and vertical mixing. TiO also has spectral features in the optical and near-infrared that have been detected. However, interpretations of TiO signatures rely on the accuracy of TiO opacity used in the models. The recently reported TOTO TiO line list provides a new opportunity to investigate these dependences, which is the goal of this work. First, we investigate how the TOTO line list affects observable transmission and emission spectra of hot Jupiters at low and high resolutions. The improvement in the TOTO line list compared to a previous line list results in observable differences in the model spectra, particularly in the optical at high resolution. Secondly, we explore the interplay between temperature structure, irradiation, and composition with TiO as the primary source of optical opacity, using 1D self-consistent atmospheric models. Among other trends, we find that the propensity for thermal inversions due to TiO peaks at  $C/O \sim 0.9$ , consistent with recent studies. Using these models, we further assess metrics to quantify thermal inversions due to TiO, compared to frequently used *Spitzer* photometry, over a range in C/O, irradiation, metallicity, gravity, and stellar type.

**Key words:** opacity – methods: numerical – techniques: spectroscopic – planets and satellites: atmospheres – planets and satellites: composition.

## 1 INTRODUCTION

In the quest to understand exoplanets in ever-increasing detail, spectroscopic observations of increasing quality are being used to study exoplanetary atmospheres. In particular, secondary eclipse spectra of transiting exoplanets provide a unique opportunity to constrain both the chemical properties and thermal structures of their day-side atmospheres (e.g. Seager et al. 2005; Burrows, Ibgui & Hubeny 2008). Both the chemical and thermal properties of an atmosphere are deeply intertwined and many works to date have aimed to shed light on the various processes that shape exoplanet emission spectra (e.g. Hubeny, Burrows & Sudarsky 2003; Fortney et al. 2006; Burrows et al. 2008; Zahnle et al. 2009; Madhusudhan 2012; Mollière et al. 2015; Parmentier et al. 2018). In particular, the

phenomenon of thermal inversions has been the focus of much work for over a decade, with approaches from both theory and observation (e.g. Hubeny et al. 2003; Burrows et al. 2008; Fortney et al. 2008; Spiegel, Silverio & Burrows 2009; Knutson, Howard & Isaacson 2010; Madhusudhan 2012; Menou 2012; Mollière et al. 2015; Beatty et al. 2017a; Parmentier et al. 2018; Gandhi & Madhusudhan 2019; Lothringer & Barman 2019).

Although thermal inversions are known to exist in the atmospheres of Solar system planets (e.g. Moses et al. 2005; Robinson & Catling 2014), the molecules that cause them (e.g. ozone in Earth’s atmosphere and hydrocarbon hazes on Jupiter) cannot exist in gas phase at the high temperatures present in hot Jupiter atmospheres. However, Hubeny et al. (2003) suggested that alternative, high-temperature, absorbers such as TiO or VO could produce thermal inversions in strongly irradiated exoplanets, opening up the field of exoplanet atmospheres to a new class of thermal structures (e.g. Fortney et al. 2006; Burrows et al. 2007).

\* E-mail: ap763@cam.ac.uk (AAAP); nmadhu@ast.cam.ac.uk (NM)

Further developments in the theory of thermal inversions have been driven by both trends observed in exoplanet emission spectra and theoretical considerations. For example, Fortney et al. (2008) suggested a two-way classification of hot Jupiters based on stellar irradiation, arguing that inversion-causing species such as TiO and VO would only be present in the gas phase for the hotter, more strongly irradiated class. This was in agreement with inferences of thermal inversions at the time, with HD 209458 b at the boundary between the two classes (Burrows et al. 2008; Knutson et al. 2008, but cf. Diamond-Lowe et al. 2014). Not all stellar irradiation aids the formation of thermal inversions, however. Knutson et al. (2010) found a negative correlation between host star activity and the presence of thermal inversions, leading them to suggest that the increased UV flux from active stars could result in the photodissociation of inversion-causing compounds and hinder the presence of thermal inversions. However, inferences of thermal inversions in some planets have since been updated, e.g. HD 209458b (see Diamond-Lowe et al. 2014).

Beyond photodissociation, there are further challenges in creating thermal inversions with TiO/VO. One is the cold trap effect, whereby these compounds condense out either on the night side or in certain (cooler) regions in the atmosphere, which can deplete the abundance of gaseous TiO/VO (Spiegel et al. 2009; Beatty et al. 2017a). Another is the fact that TiO and VO are heavy compounds relative to an H<sub>2</sub>-dominated atmosphere and will gravitationally settle if they are not kept aloft by other means (Spiegel et al. 2009). However, both of these effects could be mitigated by vertical mixing in the most irradiated atmospheres (e.g. Spiegel et al. 2009). Indeed, Parmentier, Showman & Lian (2013) find that TiO can be kept aloft in the atmosphere by vertical mixing as long as it forms sufficiently small particles when condensed on the night side.

To date, three exoplanets are known to host thermal inversions: WASP-18b (Sheppard et al. 2017), WASP-33b (Haynes et al. 2015), and WASP-121b (Evans et al. 2017). These inferences are typically made using a combination of thermal emission spectra obtained with the *HST* WFC3 spectrograph (1.1–1.7 μm) and broad-band photometry in the *Spitzer* IRAC bands at 3.6 and 4.5 μm. Whereas the *HST* WFC3 band is a good probe of H<sub>2</sub>O opacity and the spectral continuum, the IRAC 4.5 μm band has strong opacity due to CO, which is expected to be abundant in hot Jupiter atmospheres. For solar compositions and sufficiently high temperatures, the IRAC 3.6 μm band has relatively low opacity and is therefore used as a measure of the spectral continuum against which the IRAC 4.5 μm band can be compared. Under these conditions, a higher brightness temperature in the IRAC 4.5 μm band relative to the 3.6 μm band indicates the presence of a CO emission feature and an inverted temperature profile. This metric has commonly been used to assess the presence of thermal inversions in hot Jupiter atmospheres (Burrows et al. 2007; Knutson et al. 2010; Madhusudhan & Seager 2010).

On the other hand, many highly irradiated ultra-hot Jupiters (with an effective temperature of  $\gtrsim 2000$  K) have emission spectra consistent with blackbody curves in the near-infrared (e.g. Crossfield et al. 2012; Delrez et al. 2018). One explanation for this observation is an isothermal temperature profile (e.g. Crossfield et al. 2012), though an absence of strong near-infrared absorbers such as H<sub>2</sub>O would also result in a featureless spectrum in the NIR (e.g. Madhusudhan et al. 2011a). Such a depletion in H<sub>2</sub>O could be caused by either a supersolar C/O ratio (Madhusudhan 2012; Moses et al. 2013) or due to its thermal dissociation in ultra-hot Jupiters (Parmentier et al. 2018). Several recent studies also suggest that the continuum opacity in the near-infrared due to H<sup>+</sup> ions, which can exist in ultra-

hot Jupiters, could reduce the amplitude of the H<sub>2</sub>O features in the WFC3 band (e.g. Arcangeli et al. 2018; Lothringer, Barman & Koskinen 2018; Parmentier et al. 2018).

Among the factors that shape the thermal profile of an atmosphere, chemistry is a critical component. In particular, the C/O ratio has an important role in determining atmospheric chemistry, with high C/O ratios limiting the abundance of O-bearing species including H<sub>2</sub>O, TiO, and VO in hot Jupiter atmospheres (Madhusudhan et al. 2011b; Madhusudhan 2012). Here we are focusing on typical hot Jupiters orbiting Sun-like stars. Since a thermal inversion requires a high optical opacity relative to the infrared opacity (e.g. Hubeny et al. 2003; Hansen 2008; Guillot 2010), a decrease in H<sub>2</sub>O abundance due to a high C/O ratio can to some extent make it easier for a thermal inversion to occur (Mollière et al. 2015; Gandhi & Madhusudhan 2019). Furthermore, it has been found that the optical opacity causing thermal inversions may come from a variety of compounds besides TiO/VO, including sulphur compounds (Zahnle et al. 2009), Na/K (Mollière et al. 2015), H<sup>+</sup> ions (Arcangeli et al. 2018; Lothringer et al. 2018; Parmentier et al. 2018), and various oxides, hydrides, and atomic metals (Lothringer et al. 2018; Gandhi & Madhusudhan 2019). State-of-the-art observations and chemical characterization are allowing the first detections of such compounds in exoplanet atmospheres. Recent examples include detections of TiO in high resolution (Nugroho et al. 2017) and low resolution (Sedaghati et al. 2017, but cf. Espinoza et al. 2019) as well as an indication of AlO (von Essen et al. 2019), both species thought to be capable of creating thermal inversions (e.g. Hubeny et al. 2003; Fortney et al. 2008; Gandhi & Madhusudhan 2019).

These detailed chemical detections rely on the accuracy and completeness of the molecular cross-sections used to interpret spectroscopic observations (e.g. Schwenke 1998; Patrascu, Yurchenko & Tennyson 2015). While in the past, cross-sections were not designed specifically for use with exoplanet spectra, the recent need for such cross-sections has led to the development of several state-of-the-art line lists for various molecules at temperatures relevant to exoplanetary atmospheres (e.g. Rothman et al. 2010, 2013; Tennyson et al. 2016). Accurate and complete molecular cross-sections also play a key role in determining the spectral appearance and thermal profile of an atmosphere. In particular, for high-resolution spectra, line position accuracy is important as chemical detections are typically made using cross-correlation methods, which are very sensitive to line position (Balogh et al. 2012; Nugroho et al. 2017; Birkby 2018). Conversely, completeness of a line list affects the strength of spectral features in low-resolution spectra.

In this work, our goal is to explore important factors for assessing thermal inversions in the spectra of hot Jupiters. We begin by investigating the importance of up-to-date molecular cross-sections of TiO for inferring the effects of this molecule on the thermal structures and spectra of hot Jupiters. To this end, we compare the latest TiO line list, TOTO (McKemmish et al. 2019), against a previous line list (Schwenke 1998), assessing the differences they make to both transmission and emission spectra for low-resolution as well as high-resolution spectroscopic observations. We also embark on a reassessment of the criteria used for quantifying thermal inversions in hot Jupiters. Traditionally, thermal inversions have been assessed based on the relative flux differential between the *Spitzer* IRAC 1 and IRAC 2 bands at 3.6 and 4.5 μm, respectively (e.g. Knutson et al. 2008; Haynes et al. 2015; Sheppard et al. 2017; Kreidberg et al. 2018), which relies on the assumption that there is strong CO opacity in the 4.5 μm band relative to the 3.6 μm band (i.e. the 3.6 μm band is a continuum) for hot Jupiters. However, factors such as C/O ratio could affect this assumption. As a result,

the IRAC 1/IRAC 2 flux differential may not necessarily be a robust or optimal metric across all atmospheric chemistries. Furthermore, chemical properties such as the C/O ratio have also been shown to influence thermal inversions (e.g. Madhusudhan et al. 2011b; Mollière et al. 2015; Gandhi & Madhusudhan 2019), so the way in which they affect the performance of the IRAC 1/IRAC 2 metric may be non-trivial. In this study, we explore the performance of the IRAC 1/IRAC 2 metric as well as an alternative metric as a function of C/O ratio, irradiation, metallicity, and gravity.

In what follows, we begin with comparisons of different TiO line lists and their effects on model spectra under different conditions in Section 2. Here we show how the choice of line list could impact the interpretation of emission and transmission spectra at low and high resolutions. Using semi-analytic considerations of radiative equilibrium, we then explore in Section 3 how the optical versus infrared opacity varies as a function of C/O ratio and temperature, thereby assessing the dayside equilibrium temperatures at which thermal inversions could occur when TiO is a primary optical absorber. In Section 4, we assess metrics for quantifying the presence and strength of thermal inversions in the context of solar-composition atmospheres. In Section 5, we then use self-consistent atmospheric models to explore the dependence of thermal inversion strength on irradiation, C/O ratio, metallicity, and gravity. We also use these models to investigate the performance of the metrics discussed in Section 4 as a function of these atmospheric parameters. We summarize our findings and discuss our conclusions in Section 6.

## 2 IMPACT OF TIO LINE LISTS ON EXOPLANET OPACITY

Chemical cross-sections play a crucial role in interpreting atmospheric observations, and their accuracy is important to correctly infer the presence and abundance of each molecule. New observational needs, new experimental data, and new theoretical techniques have recently motivated a new line list for TiO absorption. Prior to 2019, there were two major line lists available for TiO: the Schwenke (1998) line list developed in 1998 and the Plez line list originally constructed in 1998 (Plez 1998) with the latest update in 2012 (Ryabchikova et al. 2015). These line lists were originally designed for applications in modelling M dwarfs, while now the community needs data that can model absorption by TiO in exoplanets including for ultra-high-resolution ground-based Doppler spectroscopy (e.g. Hoeijmakers et al. 2015) that demands line position accuracies better than  $\sim 0.1 \text{ cm}^{-1}$  ( $R \gtrsim 10^5$ ) for strong lines.

Fortunately, new experimental data are available for many TiO bands. These new data are combined with old data using a new algorithm called MARVEL (Császár et al. 2007; Furtenbacher, Császár & Tennyson 2007; Furtenbacher & Császár 2012) to produce accurate empirically derived energies for more than 8000 rovibronic states. Next, the new DUO (Yurchenko et al. 2016) software package is used to fit an accurate spectroscopic model of TiO with 13 electronic states based on ab initio data and these MARVEL energy levels (McKemmish et al. 2017), and then to solve this spectroscopic model to produce a large data set with over 55 million transitions and 300 000 energy levels. Finally, the energy levels are ‘MARVELIZED’, i.e. model energies are replaced with the appropriate MARVEL experimentally derived values to dramatically improve the accuracy of the predicted line positions. The resulting new TiO line list, called TOTO (McKemmish et al. 2019), covers the spectral range up to  $30\,000 \text{ cm}^{-1}$  or  $0.33 \mu\text{m}$

and is suitable for use in both modelling and detecting TiO in exoplanets.

Our results here extend the original results in McKemmish et al. (2019) in two ways: (1) quantifying the extent of ‘MARVELIZATION’ in the TOTO line list (Section 2.1) and (2) exploring the impact of different line lists on predicted hot Jupiter spectra (Sections 2.2 and 2.3).

### 2.1 Quantifying line list suitability for high-resolution spectroscopy

The importance of line list choice depends on the resolution of the observations. Fig. 1 shows the Schwenke (1998) and Plez 2012 (sourced from Ryabchikova et al. 2015) cross-sections (hereafter, S98 and P12) alongside the TOTO cross-sections in the optical and near-infrared at 2000 K, as well as the differences between them. In this spectral range, the two cross-sections differ by up to almost three orders of magnitude at native resolution and one order of magnitude when smoothed by a Gaussian point spread function (PSF) similar to that of *HST/WFC3* (see the grey and red lines in the lower panel of Fig. 1, respectively). This can have a significant impact on the interpretation of both optical and near-infrared spectra at low and high resolutions, but it is clearly much more important for high-resolution observations. In Sections 2.2 and 2.3, we focus on the differences between the TOTO and S98 cross-sections as these differ more in the optical (where TiO is most spectrally active) than the TOTO-P12 comparison, therefore providing an upper limit on the effects of these differences on hot Jupiter spectra.

The use of high-resolution Doppler spectroscopy to identify molecules in exoplanets relies on the availability of very accurate line positions. For complex molecules like TiO, the necessary accuracy can only usually be obtained if model energy levels are explicitly replaced by experimentally derived energy levels and/or transition frequencies. This replacement has not been done for the early 1998 Plez and Schwenke line lists, but it is done for the Plez 2012 line list (sourced from Ryabchikova et al. 2015) and the new TOTO line list; the former two line lists are thus not preferable for use in high-resolution cross-correlation techniques. Clear identification of the line list used in exoplanet high-resolution cross-correlation studies is thus essential for accurate chemical detections (Brogi et al. 2012; Hoeijmakers et al. 2015; Nugroho et al. 2017; Birkby 2018).

Previous studies (McKemmish et al. 2019) have compared the results of the TOTO line list to the Plez 2012 line list (sourced from Ryabchikova et al. 2015) in the context of high-resolution Doppler spectroscopy, including cross-correlation of both line lists against high-resolution M star spectra in different spectral regions. TOTO had superior performance, which can be attributed to the fact that the line list is ‘MARVELIZED’.

The extent to which a given line list explicitly includes experimental or experimentally derived (e.g. MARVEL) energy levels and/or transitions has not previously been quantified, yet this is an essential factor in determining the suitability of a given line list for use in high-resolution cross-correlation studies. Note that strong lines have the greatest contribution in the cross-correlation, so their accuracy is especially important.

The most straightforward metric is that, in TOTO, 17 365 model energy levels out of 301 245 (or 5.76 per cent) are replaced by experimentally derived MARVEL energy levels for the main isotopologue. The energy levels that are MARVELIZED, however, are the most populated energy levels; MARVELIZED energy levels contribute 95

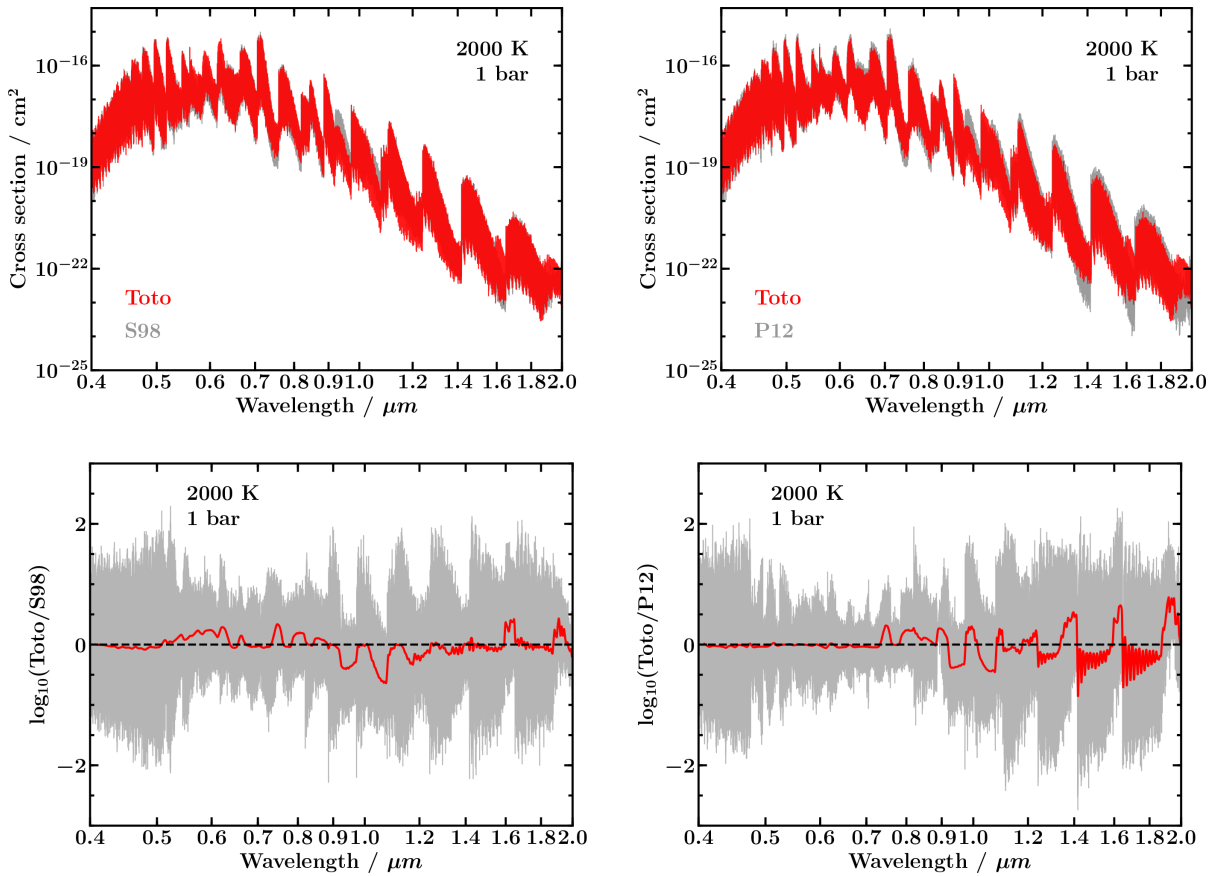


**Figure 1.** Top panels: the S98 (grey, left-hand panel)/P12 (grey, right-panel panel) and TOTO (red) cross-sections overplotted in the range 0.4–2.0  $\mu\text{m}$ . Bottom panels: the log difference between the S98 (left)/P12 (right) and TOTO cross-sections in the same wavelength range, at native resolution (grey) and smoothed with a Gaussian of width 2.3 nm (red, similar to the PSF of *HST/WFC3*). At certain wavelengths, the cross-sections differ by almost a factor of  $\sim 10$  when smoothed. The amplitudes of the residuals decrease for lower resolutions, indicating that differences in line position contribute significantly to the differences between the line lists. In all the panels, the cross-sections are taken at 2000 K and 1 bar.

and 86 per cent to the total partition function at 2000 and 3000 K, respectively.

In terms of the transitions themselves, 1373 936 out of the total 58 983 952 transitions for the main isotopologue in TOTO are between two MARVELIZED energy levels and thus have very accurately determined line positions. We can examine the importance of these transitions to the overall line list by considering Fig. 2, which shows the cross-section from only MARVELIZED transitions compared to the total TOTO line list. The completeness of the MARVEL-only data varies considerably between spectral bands with some almost entirely complete, e.g. around 0.71, 0.52, and 0.49  $\mu\text{m}$ , and some almost entirely missing, e.g. around 0.57  $\mu\text{m}$ . The most important bands missing in the MARVEL-only data involve  $v = 2$  and higher vibrational excitations of the  $B^3\Pi$  state, which have not yet been experimentally analysed; in light of their importance to high-resolution Doppler spectroscopy, these levels are thus of most importance for future experimental study.

More quantitatively, we can quantify the number of MARVELIZED transitions compared to the total number of transitions in the TOTO line list at a given temperature above a certain intensity threshold by computing stick spectra using EXOCROSS (Yurchenko et al. 2018). Approximately 83 per cent of the 4491 strongest transitions (line intensities above  $10^{-17} \text{ cm/molecule}$  at 2000 K) are MARVELIZED, with this number dropping to 64 per cent of 50 408 transitions if the threshold is chosen as  $10^{-18} \text{ cm/molecule}$ .

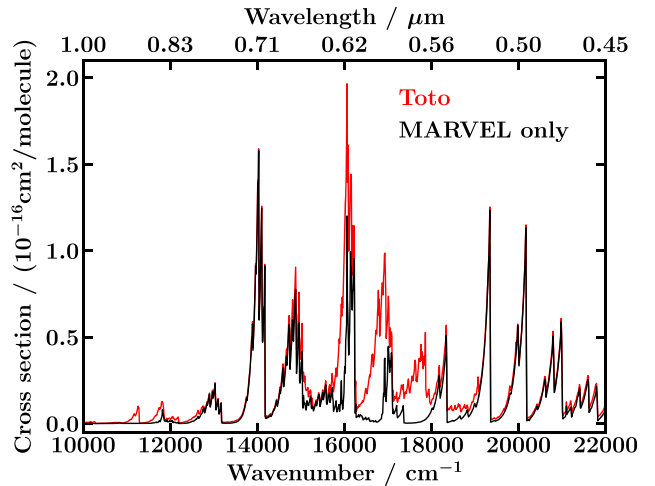


**Figure 2.** The full TOTO (red) and MARVEL-only (black) cross-sections, calculated at 2000 K using Gaussian broadening with an hwhm of  $2 \text{ cm}^{-1}$  calculated using EXOCROSS (Yurchenko, Al-Refaie & Tennyson 2018). Here, we focus on comparisons between the strongest lines as these are the regions where experimentally derived transitions are most accessible. Furthermore, it is the strongest lines that have the greatest impact on the interpretation of high-resolution Doppler spectroscopy with cross-correlation.

## 2.2 Effect of line list choice on transmission spectra

The first detections of TiO in an exoplanet atmosphere have recently been made using transit spectra (Haynes et al. 2015; Sedaghati et al. 2017). In particular, Sedaghati et al. (2017) have detected TiO in the transmission spectrum of WASP-19b [though Espinoza et al. (2019) do not detect TiO at a later epoch]. Here, we investigate the effect of the TOTO TiO line list, relative to the S98 line list, on transmission spectra by comparing two spectra for a canonical hot Jupiter. Throughout this work, model spectra are calculated for this canonical hot Jupiter using planetary/stellar properties similar to WASP-12b/WASP-12; the planetary radius and log gravity are taken as 1.79 R<sub>J</sub> and 2.989 (cgs), respectively, and the stellar radius, log gravity, [Fe/H] metallicity, and effective temperature are taken as 1.63 R<sub>⊙</sub>, 4.38 (cgs), 0.3, and 6300 K, respectively (Hebb et al. 2009; Stassun, Collins & Gaudi 2017). We generate cross-sections from the TOTO and S98 line lists using the methods described in Gandhi & Madhusudhan (2017). Using these, we generate two model transmission spectra that are identical other than the TiO cross-sections used in each. The model spectra are generated using the transmission model described in Welbanks & Madhusudhan (2019) (see also Pinhas et al. 2018). We assume an isothermal pressure–temperature (*P*–*T*) profile at 2000 K and a constant-with-depth TiO mixing ratio of 10<sup>−7</sup>. For simplicity, no other chemical species are included in these models.

The two spectra and their residuals are shown in Fig. 3. The grey line in the lower panel shows the residual for smoothed spectra; spectra in the top panel are smoothed with a Gaussian of width 0.16 nm before calculating the residual, to represent smoothing by the PSF of a ground-based instrument. At this resolution, differences of up to 400 ppm can be seen, which are comparable to observational uncertainties with current instruments. When making inferences from optical transmission spectra, choice of TiO line list can therefore have a significant impact on the conclusions drawn.

## 2.3 Effect of line list choice on emission spectra

Here, we consider the effects of the TOTO and S98 TiO cross-sections on the emission spectrum of a hot Jupiter. We do this by comparing emission spectra from two models that are identical apart from the TiO cross-sections used to generate them.

To generate these spectra, we use the GENESIS model (Gandhi & Madhusudhan 2017), which calculates full, line-by-line radiative transfer under radiative–convective equilibrium. In order to calculate equilibrium chemical abundances as a function of pressure, temperature, and elemental abundances, we use the software package HSC CHEMISTRY (version 8). This software has been used in several studies in the field of exoplanets, planet formation, and the solar nebula (e.g. Pasek et al. 2005; Bond, Lauretta & O’Brien 2010; Elser, Meyer & Moore 2012; Madhusudhan 2012; Moriarty, Madhusudhan & Fischer 2014; Harrison, Bonsor & Madhusudhan 2018), and calculates abundances by minimizing the total Gibbs free energy of the system using the GIBBS solver (White, Johnson & Dantzig 1958). We include all the chemical species used in Bond et al. (2010) and Harrison et al. (2018), plus extra ionic and molecular forms of H, O, C, N, Ti, and OH (listed in Table A1), including H<sup>−</sup>. In this section, all elemental abundances are taken to be solar.

Throughout this work, the cross-sections we use for all molecules are calculated as in Gandhi & Madhusudhan (2017) from the

HITEMP, HITRAN, and ExoMol line list data bases [H<sub>2</sub>O, CO, and CO<sub>2</sub>: Rothman et al. 2010, CH<sub>4</sub>: Yurchenko et al. 2013; Yurchenko & Tennyson 2014, C<sub>2</sub>H<sub>2</sub>: Rothman et al. 2013; Gordon et al. 2017, NH<sub>3</sub>: Yurchenko, Barber & Tennyson 2011, HCN: Harris et al. 2006; Barber et al. 2014, VO: McKemmish, Yurchenko & Tennyson 2016, collision-induced absorption (CIA): Richard et al. 2012]. We also include opacity due to Na and K (Burrows & Volobuyev 2003; Gandhi & Madhusudhan 2017). The bound-free and free–free cross-sections of H<sup>−</sup> are calculated using the prescriptions of Bell & Berrington (1987) and John (1988) (see also Arcangeli et al. 2018; Parmentier et al. 2018; Gandhi, Madhusudhan & Mandell 2020).

We also consider the effect of vertical mixing in the GENESIS code. Spiegel et al. (2009) find that TiO is heavy enough to gravitationally settle if not kept aloft by mixing, and cold traps are known to deplete TiO if it is not replenished (e.g. Burrows et al. 2007; Spiegel et al. 2009). We use a simple mixing model in which the equilibrium abundance is added to a ‘quenched’ abundance in the range 0.1–10<sup>−3</sup> bar. This ‘quenched’ value is taken to be the equilibrium abundance at 0.1 bar, where we assume that vertical mixing begins (e.g. Spiegel et al. 2009; Moses et al. 2013). The resulting abundance profile is effectively equal to the larger of the equilibrium or quenched values.

Fig. 4 shows the residuals between spectra of two otherwise identical models generated with each of the TOTO and S98 cross-sections with the *P*–*T* profile shown in the left-hand panel. The *P*–*T* profile used is a self-consistent *P*–*T* profile generated using the TOTO line list assuming a dayside equilibrium temperature of 3000 K as well as equilibrium chemistry and vertical mixing as described above. Note that we define dayside equilibrium temperature as

$$T_{\text{eq}} = \left( \frac{f}{2} \right)^{1/4} \sqrt{\frac{R_s}{a}} T_{\text{eff}}, \quad (1)$$

(henceforth, referred to as equilibrium temperature) where *f* is the fraction of incident irradiation that remains on the dayside, *R<sub>s</sub>* and *T<sub>eff</sub>* are the radius and effective temperature of the star, respectively, and *a* is the semimajor axis of the planet. Throughout this work, we assume a value of *f* = 1/2 (i.e. full redistribution of incident radiation around the planet), unless otherwise stated, and *a* is chosen such that *T<sub>eq</sub>* has the value quoted in each figure. For the incident stellar irradiation, we use ATLAS model spectra (Kurucz 1979; Castelli & Kurucz 2003) and both the stellar and planetary properties we use are listed in Section 2.2.

The spectra in Fig. 4 differ most in the optical range by up to a factor of 300 ppm. Intuitively, this is because TiO is primarily active in the optical range, and as such will have a larger impact on optical spectra. In the near-infrared, the two spectra differ by up to ∼100 ppm. However, the differences in both the optical and near-infrared are only visible at higher spectral resolutions. When the two spectra are smoothed to a resolution similar to that of *HST*/WFC3, the residuals between them are of order ∼25 ppm, which is comparable to the signal-to-noise achievable with *HST*/WFC3. When interpreting emission spectra, choice of TiO line list is therefore most important at high resolutions.

In what follows, we choose to use the TOTO cross-sections in our analysis of thermal inversions caused by TiO. In addition to the advantages discussed in Section 2.1, TOTO also has better completeness than previous line lists and takes advantage of more recent experimental data in fitting the DUO spectroscopic models (McKemmish et al. 2019).

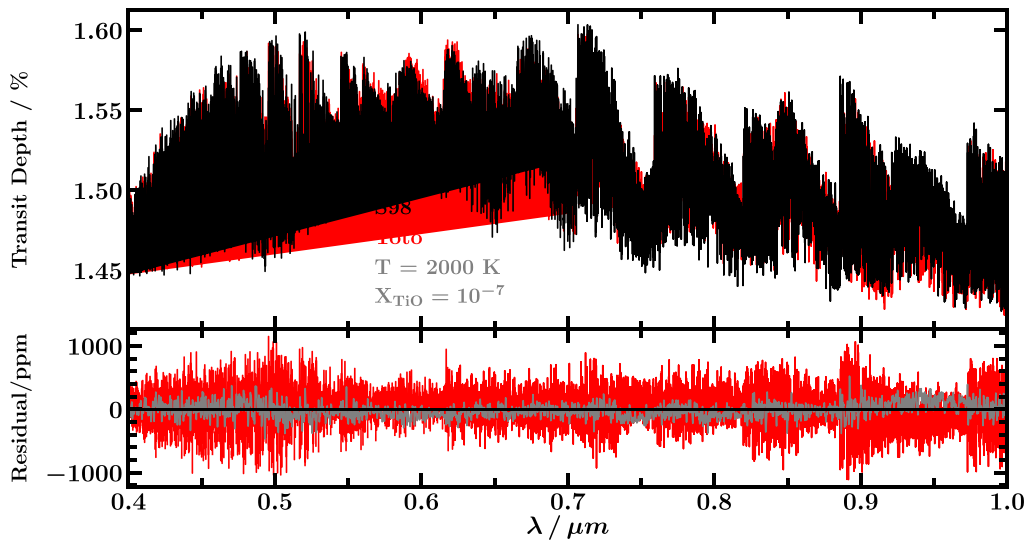


**Figure 3.** Upper panel: Transmission spectra calculated using the TOTO (red) and S98 (black) cross-sections at a resolution of  $R \sim 10000$ . The  $P-T$  profile is assumed to be an isotherm at 2000 K, and the planetary properties are those listed in Section 2. Lower panel: The red line shows the residual between the red and black spectra in the top panel (TOTO spectrum–S98 spectrum). The grey line is calculated by smoothing the red and black spectra with a Gaussian of width 0.16 nm (to represent the PSF of a ground-based instrument) and finding the residual between them.

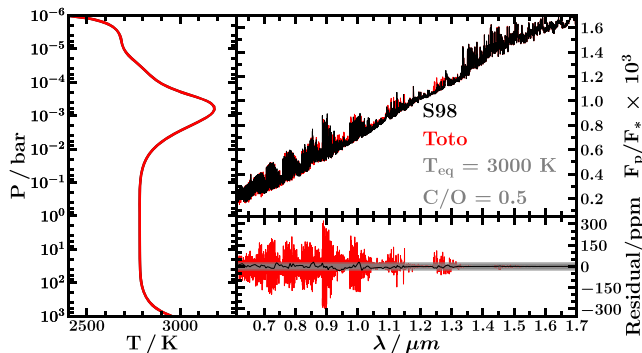


**Figure 4.** Upper right panel: spectra for two model atmospheres with identical  $P-T$  profiles, chemical profiles, irradiation, and planetary properties, but using the S98 (black) and TOTO (red) TiO cross-sections. The planetary properties are those listed in Section 2 and the semimajor axis is adjusted such that the dayside equilibrium temperature is 3000 K. Lower right panel: the residuals between the two spectra (TOTO spectrum–S98 spectrum) at a resolution of  $R \sim 10000$  (red) and smoothed with a Gaussian of width 2.3 nm (black) to represent the PSF of *HST/WFC3*. The atmospheric model used is self-consistent for the TOTO cross-sections, and the  $P-T$  profile is shown in the left-hand panel.

### 3 INFLUENCE OF CHEMISTRY ON THERMAL INVERSIONS

The thermal profile in a hot Jupiter atmosphere is dictated by the incident stellar irradiation and the sources of opacity in the atmosphere. In this section, we briefly investigate the relationship between atmospheric chemistry and temperature structure using a semi-analytic approach. A key component in determining the opacities is the abundance of each chemical species. We therefore begin by calculating equilibrium abundances for a range of chemical species as a function of temperature and C/O ratio using the HSC CHEMISTRY software as described in Section 2.3. By considering radiative equilibrium, we then use these chemical abundances to explore the range of thermal solutions that are possible under various conditions. We vary the C/O ratio by

using solar elemental abundances but varying the C abundance. In the later sections, we also vary metallicity by keeping solar elemental ratios but scaling abundances by a constant factor.

Fig. 5 shows the calculated equilibrium abundances for H<sub>2</sub>O, CO, and TiO as a function of C/O ratio and temperature. The HSC CHEMISTRY software includes the effects of condensation and thermal dissociation, which can be seen in the top panel of Fig. 5 as the abundance of TiO decreases rapidly at temperatures below  $\sim 1750$  K (condensation), and both TiO and H<sub>2</sub>O are depleted at temperatures above  $\sim 3000$  K (thermal dissociation). As expected, the abundances of both species drop by several orders of magnitude as the C/O ratio increases above unity, consistent with previous studies (Madhusudhan et al. 2011b; Madhusudhan 2012; Moses et al. 2013). In contrast, the CO abundance remains high across both low and high C/O ratios, and at cooler temperatures ( $\sim 1300$  K), CO abundance decreases as CH<sub>4</sub> takes over as the dominant carrier of carbon (Madhusudhan 2012).

These abundances affect the temperature in a region of the atmosphere through the ratio of visible to infrared opacity,  $\kappa_{\text{vis}}/\kappa_{\text{ir}}$  (Hubeny et al. 2003; Guillot 2010; Hubeny 2017).  $\kappa_{\text{vis}}$  determines the amount of incident radiation that can be absorbed, while  $\kappa_{\text{ir}}$  dictates the efficiency with which the gas is able to radiate away energy, both of which affect the steady-state temperature of the gas. These quantities are defined by

$$\begin{aligned} \kappa_{\text{vis}} &= \frac{\int_0^\infty \kappa_\nu J_\nu d\nu}{\int_0^\infty J_\nu d\nu}, \\ \kappa_{\text{ir}} &= \frac{\int_0^\infty \kappa_\nu B_\nu d\nu}{\int_0^\infty B_\nu d\nu}. \end{aligned} \quad (2)$$

$B_\nu$  is the thermal emission of the gas (a Planck function of temperature  $T$ ) and  $\kappa_\nu$  is the opacity of the gas as a function of frequency, defined as

$$\kappa_\nu = \sum_i \sigma_i n_i,$$

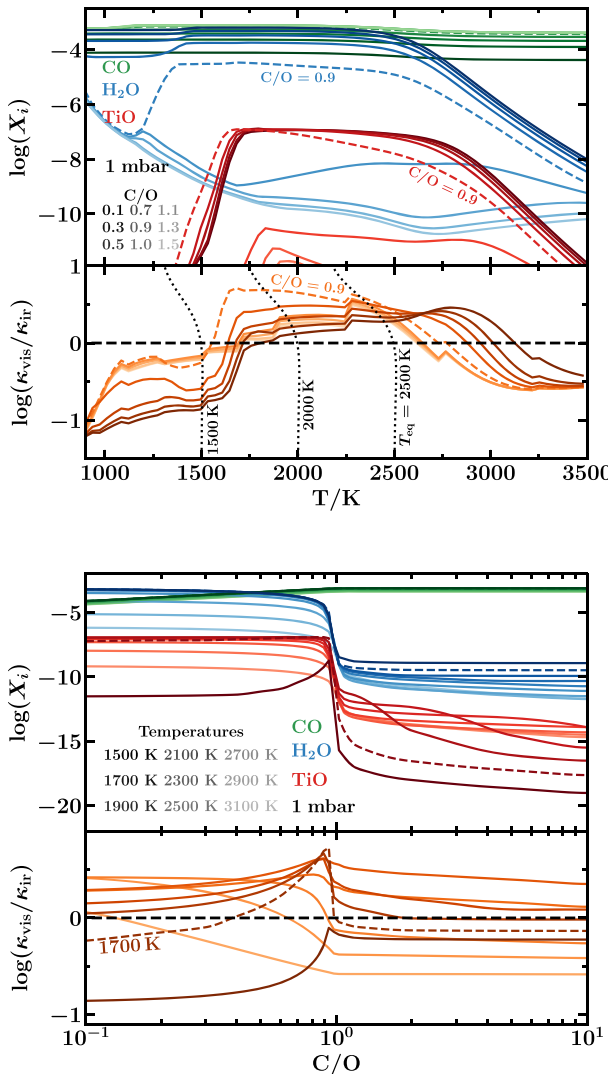


**Figure 5.** Equilibrium abundances of TiO, H<sub>2</sub>O, and CO as a function of temperature (upper section of top panel) and C/O ratio (upper section of bottom panel), for a pressure of 1 mbar. In each plot, the lower section shows the log of the ratio of optical to infrared opacities,  $\log(\kappa_{\text{vis}}/\kappa_{\text{ir}})$ . The bold black dashed lines highlight  $\kappa_{\text{vis}}/\kappa_{\text{ir}} = 1$ . Values of  $\kappa_{\text{vis}}/\kappa_{\text{ir}} \gtrsim 1$  correspond to a thermal inversion in the atmosphere. In the upper panel, the dotted black lines show  $\kappa_{\text{vis}}/\kappa_{\text{ir}}$  as a function of photospheric temperature (temperature at an optical depth of 2/3), calculated using the  $P$ - $T$  profile of Guillot (2010) and assuming equilibrium temperatures of  $T_{\text{eq}} = 1500$ , 2000, and 2500 K, respectively. In the top (bottom) panels, different line colours indicate different values of the C/O ratio (temperature), with darker shades indicating smaller values as shown by the legend. In the top panel, the dashed coloured lines correspond to C/O = 0.9, while in the bottom panel the dashed coloured lines correspond to a temperature of 1700 K. For these values,  $\kappa_{\text{vis}}/\kappa_{\text{ir}}$  has the highest peak in each plot, respectively.

where the sum is over all species and  $\sigma_i$  and  $n_i$  are the cross-section and number density of each species, respectively.  $J_\nu$  is the zeroth moment of spectral intensity of incident irradiation,  $J_\nu = \frac{1}{2} \int_{-1}^1 I_{\nu\mu} d\mu$ , where  $I_{\nu\mu}$  is the spectral intensity of incident irradiation at an angle  $\theta$  ( $\mu = \cos\theta$ ) to the local normal.

The effect of  $\kappa_{\text{vis}}/\kappa_{\text{ir}}$  on the atmospheric temperature gradient can be seen using the analytic  $P$ - $T$  profile of Guillot (2010). This profile parametrizes atmospheric temperature ( $T$ ), as a function of optical depth ( $\tau$ ), intrinsic planetary temperature ( $T_{\text{int}}$ ), dayside

temperature, and  $\kappa_{\text{vis}}/\kappa_{\text{ir}}$ . As such,  $dT/d\tau$  can be calculated as a function of  $\kappa_{\text{vis}}/\kappa_{\text{ir}}$ . Assuming a negligible  $T_{\text{int}}$ ,  $dT/d\tau$  is negative (i.e. there is a thermal inversion) when  $\kappa_{\text{vis}}/\kappa_{\text{ir}} > 1$ , for all finite values of  $\tau$  and dayside temperature (Guillot 2010; Gandhi & Madhusudhan 2019).

In Fig. 5, we show  $\kappa_{\text{vis}}/\kappa_{\text{ir}}$  as a function of C/O ratio and temperature. For simplicity, we use a single pressure of 1 mbar to represent the upper atmosphere. To calculate  $\kappa_{\text{vis}}/\kappa_{\text{ir}}$ , we include opacity contributions from TiO, H<sub>2</sub>O, CH<sub>4</sub>, NH<sub>3</sub>, CO, CO<sub>2</sub>, HCN, C<sub>2</sub>H<sub>2</sub>, Na, K, VO, and CIA, using equilibrium chemical abundances from HSC CHEMISTRY. From Fig. 5 (top panel), we see that  $\kappa_{\text{vis}}/\kappa_{\text{ir}}$  only has values above unity for temperatures greater than  $\sim 1500$ . This suggests that thermal inversions caused by TiO can only occur for atmospheric temperatures above 1500 K. This temperature limit corresponds to C/O = 0.9, while lower and higher C/O ratios begin to exceed  $\kappa_{\text{vis}}/\kappa_{\text{ir}}$  only at higher temperatures. Larger values of  $\kappa_{\text{vis}}/\kappa_{\text{ir}}$  coincide with larger values of TiO abundance, which is expected since TiO is a primary visible absorber in this scenario. Outside the range of large  $\kappa_{\text{vis}}/\kappa_{\text{ir}}$ , condensation and thermal dissociation of TiO both diminish its value at low and high temperatures, respectively. Na and K can also contribute significantly to the optical opacity, and hence thermal inversions, for C/O  $\gtrsim 1$  (see also Mollière et al. 2015). For example, at C/O  $\geq 1$ , where TiO is strongly depleted, optical opacity due to Na and K results in  $\kappa_{\text{vis}}/\kappa_{\text{ir}} > 1$  for temperatures greater than  $\sim 1750$  K.

We can use  $\kappa_{\text{vis}}/\kappa_{\text{ir}}$  as shown in Fig. 5 to broadly assess the feasibility of thermal inversions for a given  $T_{\text{eq}}$ . To do this, we again use the analytic temperature profile from Guillot (2010), setting  $\tau = 2/3$  (i.e. corresponding to the photosphere) and assuming that intrinsic heat is negligible compared to the irradiation. For a chosen equilibrium temperature, this results in a relation between  $\kappa_{\text{vis}}/\kappa_{\text{ir}}$  and photospheric temperature. This is shown by the dotted black lines in the upper panel of Fig. 5 for three equilibrium temperatures (1500, 2000, and 2500 K). Solutions for the photospheric temperature occur at the intersection points between these lines and the values of  $\kappa_{\text{vis}}/\kappa_{\text{ir}}$  calculated independently from the molecular opacities (coloured lines in the lower section of the upper panel in Fig. 5). Where these intersections happen at  $\kappa_{\text{vis}}/\kappa_{\text{ir}} > 1$ , a thermal inversion is possible.

Fig. 5 therefore shows that inversions start to become possible at temperatures in the range  $\sim 1500$ –2000 K, depending on the C/O ratio. For example, for C/O = 0.9, thermal inversions are possible at equilibrium temperatures just above 1500 K, while for C/O  $\geq 1.0$  equilibrium temperatures  $\gtrsim 1750$  K are required. This is comparable to the equilibrium temperature at which Fortney et al. (2008) begin to see thermal inversions for a Sun-like host star ( $\sim 1800$  K). To fully understand the effects of equilibrium chemical abundances on the  $P$ - $T$  profile of an atmosphere, we extend our analysis with full numerical atmospheric models in Section 5.

#### 4 METRICS FOR ASSESSING THERMAL INVERSIONS

In this section, we assess metrics for inferring the presence and strength of thermal inversions in exoplanet atmospheres with solar-like compositions. A common way to do this involves comparing two photometric measurements, e.g. using the *Spitzer* IRAC 1 and IRAC 2 channels (e.g. Burrows et al. 2007; Knutson et al. 2010; Madhusudhan & Seager 2010). Assessing the presence of a thermal inversion with two or more spectral or photometric bands requires at least one band that probes a high-opacity region of the spectrum and an opacity window that probes as little line opacity as possible, i.e.

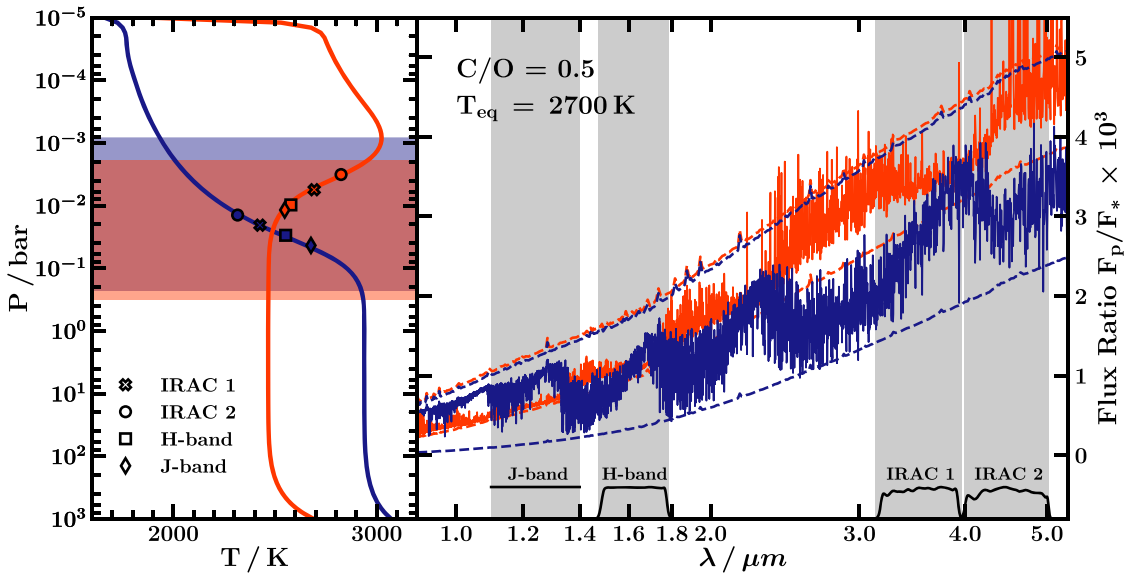


**Figure 6.** Temperatures and pressures probed by the  $J$ ,  $H$ , IRAC 1 and IRAC 2 photometric bands. Red and blue spectra in the right-hand panel correspond to the  $P$ - $T$  profiles of the same colour in the left-hand panel; both are generated using the properties listed in Section 2 and the red spectrum includes TiO while the blue one does not. Markers in the left-hand panel show the brightness temperatures (and corresponding pressures) of the IRAC 1, IRAC 2,  $H$ -band, and  $J$ -band photometric points from each of the spectra, respectively. Each of these bands is shown by the grey shaded regions in the right-hand panel and their transmission functions are shown in black. The blue and red shaded regions in the left-hand panel show the pressure ranges of the photospheres for the blue and red  $P$ - $T$  profiles, respectively.

a spectral continuum. The continuum band probes deeper regions of the atmosphere while the high-opacity band probes higher up in the atmosphere. The difference in brightness temperature between these bands provides a measure of the temperature gradient in the photosphere. While a ‘perfect’ opacity window would contain no line opacity at all, this is not realistic. Furthermore, continuum opacity such as CIA opacity is itself wavelength dependent. Therefore, different continuum bands can have varying levels of both line opacity contamination and continuum opacity. A continuum band with less line opacity probes deeper into the atmosphere and therefore has the potential to probe a larger temperature contrast when compared to the ‘high-opacity’ band. Therefore, when looking for metrics to assess thermal inversions it is advantageous to consider the clearest possible continuum bands. For example, Stevenson (2016) use the  $J$  band as a continuum compared to a water absorption band when quantifying absorption features in transmission spectra.

The IRAC 1 and IRAC 2 channels (at  $3.6$  and  $4.5$   $\mu\text{m}$ , respectively) are commonly used to infer the presence of thermal inversions in hot Jupiters as the  $3.6$   $\mu\text{m}$  band does not contain very strong molecular features for solar-composition atmospheres while the  $4.5$   $\mu\text{m}$  band probes a strong CO feature (e.g. Burrows et al. 2007; Knutson et al. 2009; Madhusudhan & Seager 2010). This property has also been used to construct colour-magnitude diagrams for exoplanets and brown dwarfs and to subsequently compare irradiated exoplanets to other types of sub-stellar object (Triaud 2014; Triaud et al. 2014). For a hot Jupiter with solar composition and a thermal inversion, the brightness temperature contrast between the IRAC 2 and IRAC 1 channels,  $T_{4.5\,\mu\text{m}} - T_{3.6\,\mu\text{m}}$ , is expected to be positive. On the other hand, an atmosphere with solar composition but without a thermal inversion would be expected to have  $T_{4.5\,\mu\text{m}} - T_{3.6\,\mu\text{m}} < 0$ . However, in reality, the IRAC 1 band is not a perfect opacity window. In particular, it has contributions from CH<sub>4</sub>, H<sub>2</sub>O, and HCN (Madhusudhan 2012). This is particularly evident for high C/O ratios close to 1 where

CH<sub>4</sub> and HCN can have significant opacity contributions. Under such circumstances, an atmosphere without a thermal inversion can still have significantly low flux in the IRAC 1 band due to CH<sub>4</sub> and/or HCN absorption compared to the IRAC 2 band with CO. This situation can give rise to a positive  $T_{4.5\,\mu\text{m}} - T_{3.6\,\mu\text{m}}$  contrast that can mimic the behaviour of a thermal inversion (Section 5.2). Other photometric bands may therefore provide a better opacity window compared to the IRAC 1 channel, and planets with different chemistries may require different bands to probe the spectral continuum.

Here, we use theoretical models to assess metrics for temperature gradients in atmospheres with solar-like compositions. We calculate brightness temperatures using the method described by Garhart et al. (2020); for a spectral bin in the wavelength range  $\lambda_{\min} - \lambda_{\max}$  and a normalized instrument sensitivity function  $\zeta$ , the brightness temperature,  $T_b$ , is chosen such that

$$\int_{\lambda_{\min}}^{\lambda_{\max}} \pi \zeta B_\lambda(T_b) d\lambda = \frac{F_p}{F_s} \frac{R_s^2}{R_p^2} \times \int_{\lambda_{\min}}^{\lambda_{\max}} \pi \zeta I_s d\lambda,$$

where  $\frac{F_p}{F_s}$  is the observed planet-star flux ratio in the photometric band,  $\pi I_s$  is the stellar surface flux [we use ATLAS model spectra: Kurucz (1979) and Castelli & Kurucz (2003)], and  $R_p$  is the planetary radius.

We begin by investigating optimal continuum bands for hot Jupiter atmospheres of solar composition. In particular, we compare the  $H$  and  $J$  bands to the IRAC 1 band according to their performance as continuum bands for solar-composition spectra (see Fig. 6). Both the  $H$  and  $J$  bands coincide with local minima in H<sub>2</sub>O opacity, so, for spectra dominated by H<sub>2</sub>O, they should probe deeper regions of the atmosphere relative to bands that probe stronger features (Stevenson 2016). We demonstrate this property here using two self-consistent atmospheric models for which the  $P$ - $T$  profiles and spectra are shown in Fig. 6. Both models are generated using the GENESIS self-consistent modelling code (Gandhi & Madhusudhan

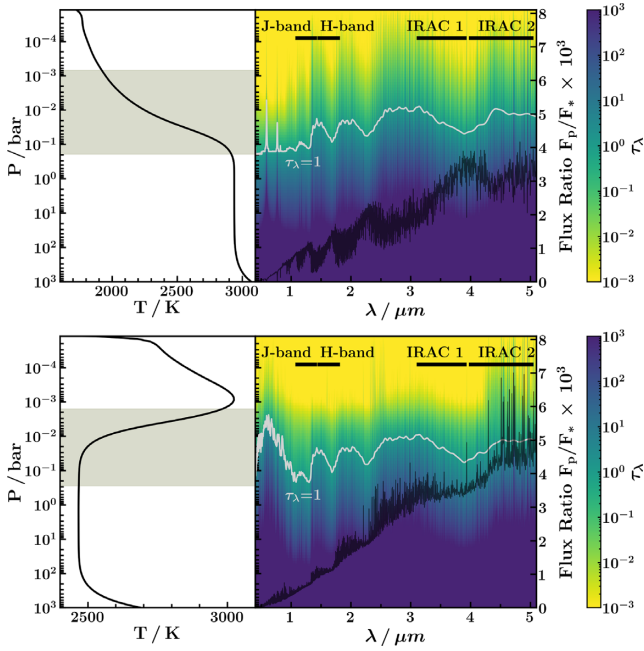


**Figure 7.** Optical depth as a function of wavelength and pressure (i.e. altitude) in the atmosphere for the two  $P$ – $T$  profiles shown in Fig. 6. The left-hand panels show the  $P$ – $T$  profile with the photosphere (calculated as the extent of the  $\tau=1$  surface) shaded in grey. In the right-hand panels, the  $\tau=1$  surface is shown as a function of wavelength and pressure by the grey line. Opacity windows, including the  $J$ ,  $H$ , and IRAC 1 bands, occur where the optical depth reaches unity at deeper pressures. The emergent spectrum of the planet is shown in black. The horizontal black lines indicate the  $J$ ,  $H$ , IRAC 1, and IRAC 2 bands.

2017). The equilibrium chemical abundances are calculated using HSC CHEMISTRY assuming a C/O ratio of 0.5. The model shown in blue does not include TiO and has a non-inverted profile, while the model shown in red does include TiO and has a thermal inversion. For each model, we compute a simulated photometric measurement for each of the four bands mentioned above, and calculate the brightness temperature of each measurement. These temperatures are plotted over the  $P$ – $T$  profiles in the left-hand panel of Fig. 6 and indicate which part of the photosphere is probed by each band.

We find that the  $H$  and  $J$  bands probe deeper atmospheric pressures compared to the IRAC 1 band for these models. This is clearly demonstrated in Fig. 7, which shows optical depth as a function of wavelength and pressure in the atmosphere (i.e. altitude). The  $J$ ,  $H$ , and IRAC 1 bands all correspond to windows in opacity, where optical depth reaches unity at deeper pressures. However, in the  $J$  and  $H$  bands, unit optical depth is reached at pressures of  $\sim 1$  order of magnitude greater than that for the IRAC 1 band. Fig. 7 also shows that deeper pressures can be probed at higher spectral resolutions by sampling very narrow windows in opacity and avoiding contamination from higher opacity regions. We demonstrate this concept in greater detail in Appendix B (see also de Kok et al. 2014). Despite this effect, wider photometric bands are still observationally favourable as they are less sensitive to small wavelength shifts in the detector.

Since, in the cases shown here, the  $J$  and  $H$  bands are better opacity windows than the IRAC 1 band, the brightness temperature contrasts between the IRAC 2 channel and the  $H$  band ( $T_{4.5\mu\text{m}} - T_H$ ) or between the IRAC 2 channel and the  $J$  band ( $T_{4.5\mu\text{m}} - T_J$ ) are greater than the contrast between the two IRAC channels

( $T_{4.5\mu\text{m}} - T_{3.6\mu\text{m}}$ ). For both the inverted and non-inverted model  $P$ – $T$  profiles, an inversion/non-inversion could be inferred based on the brightness temperatures of the IRAC 2 channel and any of the other three bands, since the IRAC 2 channel probes the shallowest pressures (highest altitudes) in both cases, corresponding to the hottest/coolest brightness temperature for the inverted/non-inverted profile. However, a larger brightness temperature contrast provides more information about the atmospheric temperature gradient and can potentially allow for a more robust inference of an inversion/non-inversion. In this case, the  $J$  band would therefore be the best suited for comparison to the IRAC 2 band, as it probes deeper into the atmosphere. Although the  $H$  and  $J$  bands may not be optimal probes of the continuum for spectra that are not dominated by  $\text{H}_2\text{O}$  opacity, this demonstrates that it can be beneficial to consider bands other than the IRAC 1 channel when seeking to determine the presence of a thermal inversion based on photometric measurements alone. In Section 5, we extend this assessment to a wider range of C/O ratios, equilibrium temperatures, metallicities, gravities, and stellar types.

## 5 METRICS AS A FUNCTION OF PLANETARY AND HOST STAR PROPERTIES

In this section, we use self-consistent models to investigate in detail how chemical composition, incident irradiation, and gravity affect the strength of thermal inversions in hot Jupiters as well as the performance of temperature gradient metrics. We use the GENESIS code (Gandhi & Madhusudhan 2017) to generate self-consistent model atmospheres and their spectra for various C/O ratios, equilibrium temperatures, metallicities, stellar types, and gravities. The equilibrium chemical abundances are calculated with HSC CHEMISTRY, and we also include the effects of vertical mixing by quenching all chemical abundances between 0.1 and  $10^{-3}$  bar (see Section 2.3). In addition to vertical mixing, we also consider the redistribution of incident flux to the night side of the planet. Following Garhart et al. (2020), we approximate the redistribution factor,  $f$ , as a step function where planets with  $T_{\text{eq}} \leq 2500$  K transport 50 per cent of incident flux to the night side ( $f = 1/2$ ), while planets with  $T_{\text{eq}} > 2500$  K retain all incident energy on the dayside ( $f = 1$ ) (see also Cowan & Agol 2011).

Using these equilibrium models, we calculate  $P$ – $T$  profiles and model spectra for a range of  $T_{\text{eq}}$ , C/O ratios, metallicities, stellar types, and gravities. Since we are focusing on thermal inversions due to TiO, we explore C/O ratios  $\leq 1$  as TiO is significantly depleted at higher C/O ratios. The opacity sources we include in our models are those listed in Section 2.3. We note that other sources of optical opacity not considered here (e.g. atomic Fe and Mg; Lothringer & Barman 2019) can also cause thermal inversions, though we focus on thermal inversions due to TiO in this work. We then use these models to explore temperature gradient as a function of these parameters, and compare different empirical metrics for assessing this gradient. In order to test the performance of the empirical metrics, we compare them to the true temperature gradient derived from the model  $P$ – $T$  profiles. This is found by considering the temperature contrast across the photosphere, which we take to be in the range  $1\text{--}10^{-3}$  bar. For highly irradiated atmospheres, it is well known that the temperature profile becomes isothermal in the high optical depth limit before becoming steeper again at even higher pressures (Guillot 2010). Note that, since we are using an internal temperature of 100 K that is much smaller than the irradiation temperature, the isotherm extends to the bottom of our computational domain and we do not

see the steeper gradient. For the dayside of irradiated atmospheres such as those modelled here, the base of the photosphere coincides with the top of this isotherm in the lower atmosphere (e.g. Hubeny et al. 2003; Burrows, Sudarsky & Hubeny 2006; Guillot 2010). The temperature of the isotherm is therefore a consistent measure of the temperature at the bottom of the photosphere across all the models we consider. For profiles with a thermal inversion, the temperature contrast is defined as the maximum photospheric temperature minus the minimum temperature between the bottom of the photosphere ( $\sim 1$  bar) and the location of the temperature maximum. For profiles with no inversion, the contrast is defined as the minimum atmospheric temperature minus the temperature at the bottom of the photosphere (at 1 bar, i.e. the temperature of the isotherm). We consider a  $P$ - $T$  profile to have a thermal inversion if the inversion strength is greater than 30 K. Maps of inversion strength as a function of C/O ratio and equilibrium temperature are shown in Figs 8, 9, and 10 for varying metallicities, stellar host types, and planetary surface gravities.

### 5.1 Inversion strength

The true temperature contrasts shown in the top rows of Figs 8, 9, and 10 show that a wide variety of  $P$ - $T$  profiles are possible in this parameter space, including strong thermal inversions, isotherms, and non-inverted profiles. This is in accordance with observations of hot Jupiters, which have revealed spectra with emission features (e.g. Haynes et al. 2015; Evans et al. 2017; Sheppard et al. 2017; Arcangeli et al. 2018), flat spectra (e.g. Swain et al. 2013; Cartier et al. 2017; Mansfield et al. 2018), and absorption features (e.g. Beatty et al. 2017b). We also plot contours of  $\kappa_{\text{vis}}/\kappa_{\text{ir}} = 1$  (calculated at a nominal pressure of 1 mbar) in the top panels of Fig. 8 to show the regions of parameter space expected to host thermal inversions (Section 3). Note, however, that these contours do not include effects due to vertical mixing and are only calculated at a single pressure, whereas thermal inversions can happen at different pressures for different cases. Nevertheless, the  $\kappa_{\text{vis}}/\kappa_{\text{ir}} = 1$  contours roughly outline the regions of the parameter space where thermal inversions occur.

The models in Figs 8, 9, and 10 suggest that strong inversions are more likely to occur at higher C/O ratios in the  $\text{C}/\text{O} < 1$  regime, as has been previously discussed in other works (e.g. Mollière et al. 2015; Gandhi & Madhusudhan 2019). This is consistent with the trend seen in Section 3 and in the  $\kappa_{\text{vis}}/\kappa_{\text{ir}} = 1$  contour that thermal inversions are possible for a C/O of 0.9 at a lower equilibrium temperature compared to other C/O ratios. In addition, for a C/O ratio of one, only weak thermal inversions or non-inverted profiles are seen in the models, consistent with the strong depletion of TiO at  $\text{C}/\text{O} = 1$  (Madhusudhan et al. 2011b). As discussed in Section 3, these thermal inversions are caused by optical opacity from Na and K (also see e.g. Mollière et al. 2015) as TiO abundance is strongly depleted for  $\text{C}/\text{O} \geq 1$  (e.g. Madhusudhan 2012).

Another clear trend is that for increasing metallicity, peak inversion strength occurs at higher  $T_{\text{eq}}$  (Fig. 8). This is because TiO is depleted by condensation and thermal dissociation at relatively higher temperatures for higher metallicity (Fig. C1), so a higher equilibrium temperature is needed to obtain  $\kappa_{\text{vis}}/\kappa_{\text{ir}} = 1$  [see Appendix C and Mollière et al. (2015)]. Furthermore, the strongest thermal inversions are stronger for high-metallicity models, as seen in Fig. 8. Compared to variation in metallicity, changes in stellar type have a more subtle effect on thermal inversion strength in the parameter space tested here. However, Fig. 9 does show that

earlier stellar types can allow somewhat stronger thermal inversions, e.g. inversion strengths for a K7V host star are typically weaker compared to F6V and G0V host stars in this parameter space (see also Lothringer & Barman 2019). Furthermore, a later stellar type can allow thermal inversions to occur at lower equilibrium temperatures. In particular, for the K7V host star, thermal inversions start to become possible at 1750 K and  $\text{C}/\text{O} = 0.7\text{--}0.8$ , which is not the case for the F6V and G0V host stars.

We also test the effect of increasing the planetary surface gravity in Figs 8 and 10. In the centre column of Fig. 8, the surface gravity is chosen to be similar to WASP-12b [ $\log(g/\text{cm}^{-2}) = 2.99$ ], while in Fig. 10 we use a larger gravity similar to WASP-18b [ $\log(g/\text{cm}^{-2}) = 4.26$ ]. Between these two extremes, there are only minimal differences in inversion strength in the parameter space investigated here. One difference is that in the high-gravity case, slightly higher inversion strengths are typically found for lower  $T_{\text{eq}}$  and lower C/O ratio. There are also a few cases for which the high- and low-gravity models disagree on the presence of a thermal inversion. However, the  $P$ - $T$  profiles in these cases are in fact similar between the high- and low-gravity models, and the difference in inversion classification is due only to small differences between the profiles. Since the two gravities investigated here are extremes of the range expected for hot Jupiters, we conclude that gravity has a relatively small impact on inversion strength compared to factors such as metallicity. We also note that in our models, the gravity impacts the thermal profile only through the scale height and the fact that the photosphere is at higher pressure and therefore has greater pressure broadening of the chemical cross-sections. However, a varying gravity could impact the gravitational settling of heavier species such as TiO, which we do not consider here (Beatty et al. 2017a).

### 5.2 Performance of metrics

We also use these models to test the performances of the *Spitzer* and *J*-band metrics discussed in Section 4. As discussed in Section 4, each of the photometric bands used by these metrics probes either a spectral feature (i.e. the IRAC 2 band) or a spectral window (e.g. the IRAC 1 and *J* bands), allowing different pressures in the atmosphere to be probed. In Section 4, the efficacy of these bands in probing spectral features and windows was explored for a solar-like composition and a single equilibrium temperature. Here, we extend this analysis to a range of C/O ratios, equilibrium temperatures, metallicities, stellar types, and gravities. Fig. 8 shows brightness temperature contrasts for these metrics between equilibrium temperatures of 1500–3000 K, for C/O ratios of 0.1–1.0, and for metallicities of 0.1, 1, and  $10\times$  solar. The middle row of Fig. 8 shows brightness temperature contrasts between the *Spitzer* IRAC 1 and IRAC 2 bands,  $T_{4.5\,\mu\text{m}} - T_{3.6\,\mu\text{m}}$ , while the bottom row shows the  $T_{4.5\,\mu\text{m}} - T_{\text{J}}$  contrast. Similarly, these contrasts are shown for different stellar types (K7V, F6V, and G0V) and planetary gravities in Figs 9 and 10, respectively.

Across the parameter space we explore, the IRAC 2 channel probes a CO spectral feature, as CO is abundant at all of the temperatures and C/O ratios modelled (Fig. 5). However, the spectral features or windows probed by the IRAC 1 and *J* bands can vary depending on chemistry. For example, the IRAC 1 band coincides with CH<sub>4</sub> and HCN opacity features. Therefore, for an atmosphere with high CH<sub>4</sub> and/or HCN abundance, the IRAC 1 band will no longer probe a spectral window and the performance of the *Spitzer* metric may not be optimal. This can be seen in Figs 8, 9, and 10 at low equilibrium temperatures ( $T_{\text{eq}} \approx 1500$  K) and high

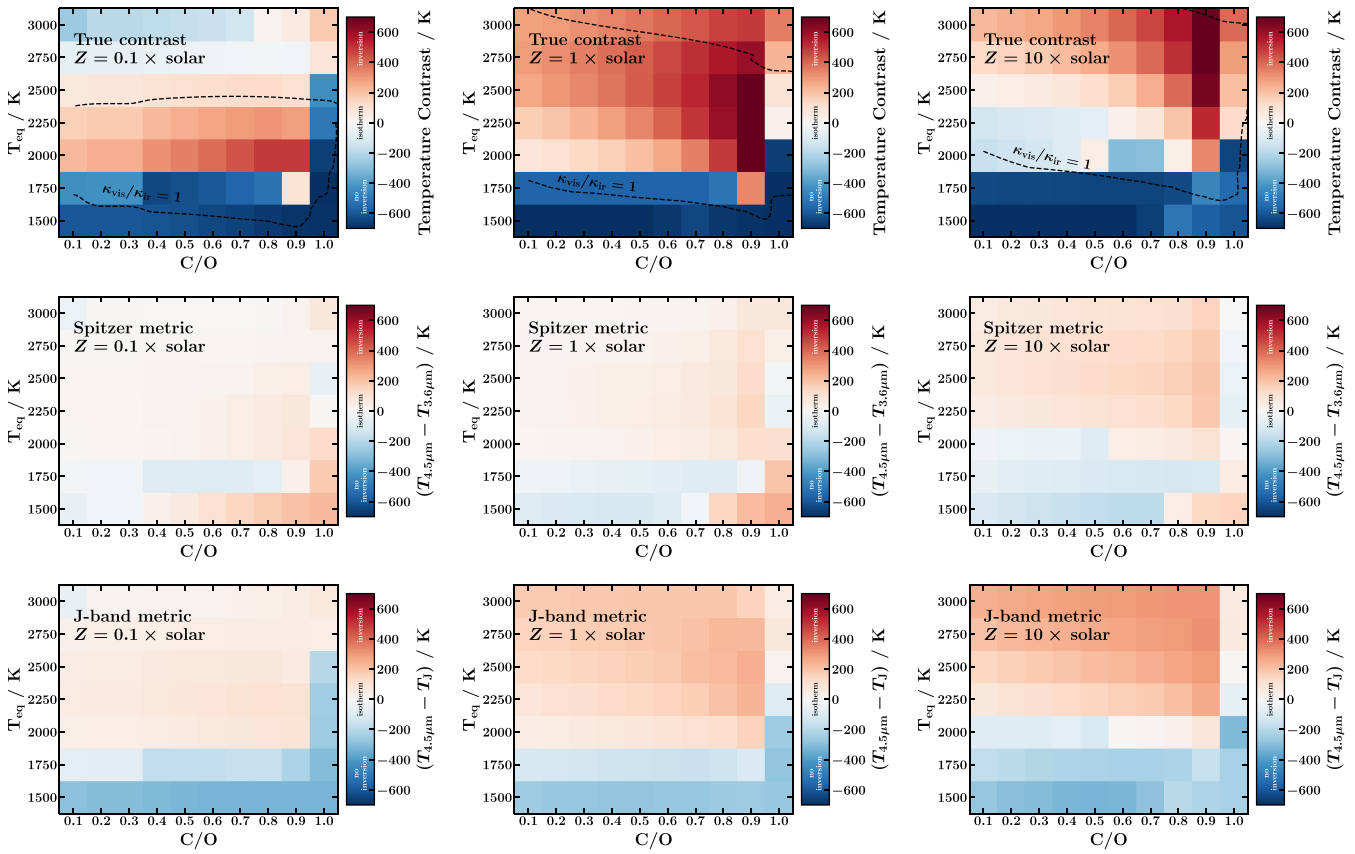


**Figure 8.** Inversion maps showing the strength of the inversion/non-inversion of equilibrium  $P$ - $T$  profiles as a function of equilibrium temperature and C/O ratio. Equilibrium  $P$ - $T$  profiles are calculated as described in Section 2. The left, middle, and right columns correspond to metallicities of 0.1, 1, and  $10 \times$  solar, respectively. Top row: colour scale shows temperature contrast within the pressure range  $1\text{--}10^{-3}$  bar (see Section 5 for definition of the temperature contrast). The dashed black line shows contour of  $\kappa_{\text{vis}}/\kappa_{\text{ir}} = 1$  at a pressure of 1 mbar (see Section 3). This predicts that models inside the contour should have thermal inversions, though note that this contour does not include effects due to vertical mixing and does not account for the fact that thermal inversions can happen at different pressures for different cases. Middle and bottom rows: performance of the *Spitzer* and *J*-band metrics throughout the parameter space. Colour scale shows brightness temperature contrasts between the IRAC 1 and IRAC 2 bands ( $T_{4.5\,\mu\text{m}} - T_{3.6\,\mu\text{m}}$ , middle row) and between the *J* band and IRAC 2 band ( $T_{4.5\,\mu\text{m}} - T_J$ , bottom row). Positive (negative) values indicate a thermal inversion (non-inversion).

C/O, where  $T_{4.5\,\mu\text{m}} - T_{3.6\,\mu\text{m}}$  has positive values, despite the lack of thermal inversion in the models in this region of parameter space. Overall, the *J*-band metric provides a slightly better match to the true contrast than the IRAC 1 band. However, since the *J* band is chosen as a continuum relative to  $\text{H}_2\text{O}$  absorption, the *J*-band metric will not necessarily work for atmospheres that are water poor, e.g. for  $\text{C}/\text{O}>1$  or other compositions not considered here. We explore this phenomenon further in Section 5.3.

While the *Spitzer* and *J*-band metrics largely agree as to whether an inversion is present or not, there are two main exceptions to this trend. The first is at low equilibrium temperatures and high C/O, for reasons described above. The second is at  $T_{\text{eq}} \sim 1750$  K where, for some C/O ratios, the *J* band incorrectly infers a non-inversion. For example, this occurs with a K7V host star (Fig. 9). Nevertheless, the two metrics agree for most  $T_{\text{eq}}$  and C/O ratios. This is consistent with the fact that our analysis is for oxygen-rich compositions where  $\text{H}_2\text{O}$  absorption dominates and the *J* band and IRAC 1 band do indeed probe the continuum. Furthermore, where this agreement exists, the  $T_{4.5\,\mu\text{m}} - T_J$  contrast is consistently larger than the  $T_{4.5\,\mu\text{m}} - T_{3.6\,\mu\text{m}}$  contrast. This effect is visible in Fig. 6 for a solar-like composition, and Figs 8, 9, and 10 confirm that it holds across the range of  $T_{\text{eq}}$ , C/O ratios, metallicities, stellar

types, and gravities explored here. This suggests that, as in Fig. 6, the *J* band is consistently probing deeper pressures than the IRAC 1 band. For an oxygen-rich atmosphere with a thermal inversion, one would therefore expect that  $T_J < T_{3.6\,\mu\text{m}} < T_{4.5\,\mu\text{m}}$ . Similarly,  $T_{4.5\,\mu\text{m}} < T_{3.6\,\mu\text{m}} < T_J$  would be expected for an oxygen-rich atmosphere with no thermal inversion. In Section 5.3, we compare these brightness temperatures for hot Jupiters with spectral and photometric observations. By looking for outliers to this trend, we can therefore identify which planets have different chemistries or disequilibrium processes compared to those we consider in our models.

### 5.3 Comparison of data to models

While we have so far discussed photometric bands for assessing thermal inversions in oxygen-rich spectra, we now consider a more general approach by directly considering brightness temperatures probed by existing data. We do this by plotting the brightness temperatures of *HST/WFC3* and *Spitzer* IRAC 1 and IRAC 2 observations for seven planets (Fig. 11). Here, we choose to use IRAC 1 and IRAC 2 brightness temperatures from Garhart et al.

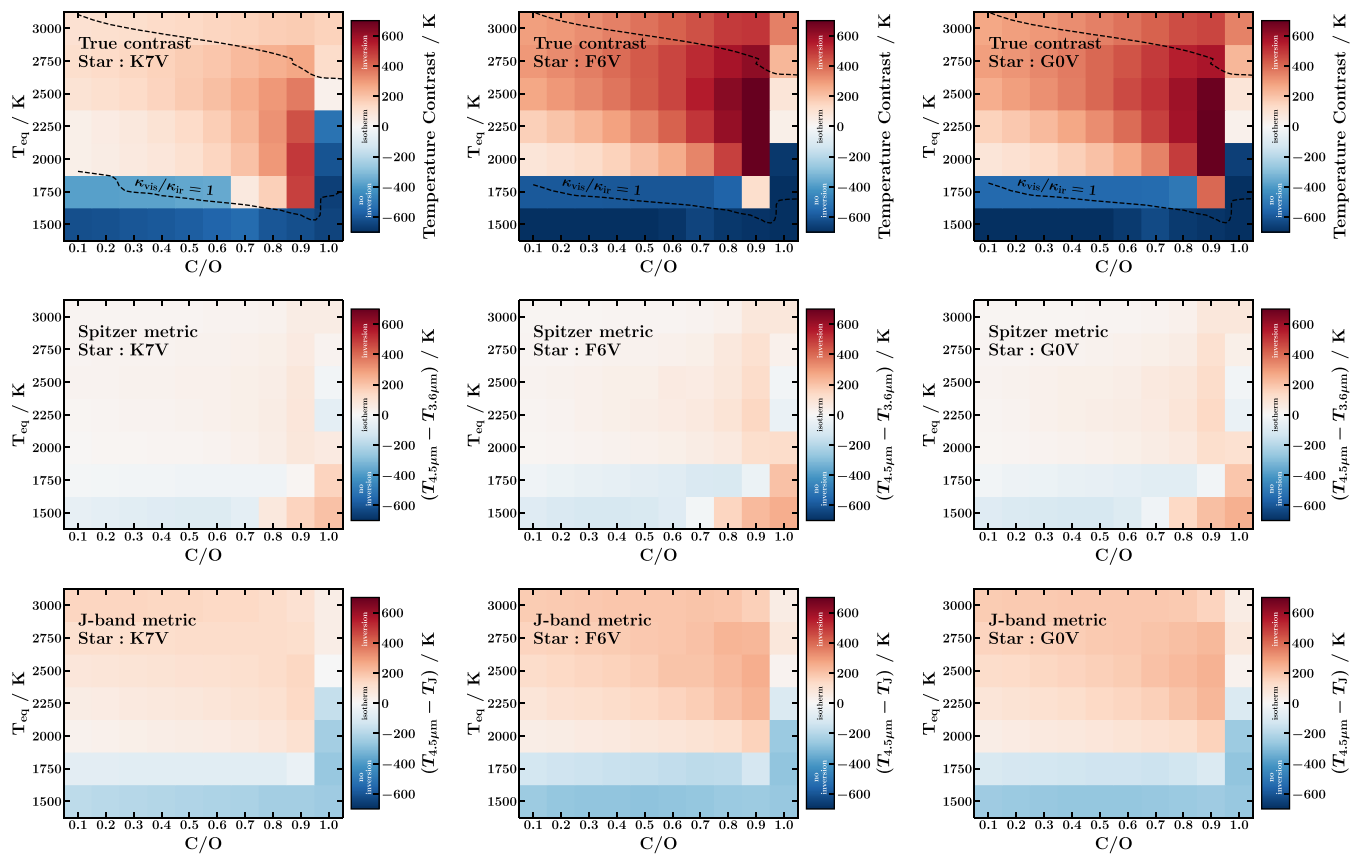


**Figure 9.** Inversion strength as a function of equilibrium temperature, C/O ratio, and stellar type of the host star. The left, middle, and right columns correspond to the stellar types K7V, F6V, and G0V, respectively. The stellar properties used for each stellar type are those of WASP-43, WASP-18, and HD 209458, respectively (Hellier et al. 2011; Southworth 2012; Stassun et al. 2017). Colour scales show the same temperature contrasts as in Fig. 8. Contours of  $\kappa_{vis}/\kappa_{ir} = 1$  in the top row are calculated in the same way as for Fig. 8 but using the appropriate host star temperature for each case.

(2020) as they perform a uniform analysis across many *Spitzer* secondary eclipse observations. However, we note that the *Spitzer* data for a given object can differ depending on the way it is analysed [e.g. Garhart et al. (2020) compared to Kreidberg et al. 2018].

As discussed in Section 5, oxygen-rich atmospheres are expected to have  $T_J < T_{3.6\mu m} < T_{4.5\mu m}$  or  $T_{4.5\mu m} < T_{3.6\mu m} < T_J$  for cases with and without a thermal inversion, respectively, and under the assumptions of our models (e.g. chemistry and prescriptions for vertical mixing). Here, we investigate whether the planets in Fig. 11 also exhibit this trend. To do this, we use *HST*/WFC3 brightness temperatures in the  $J$  band as a proxy for  $J$ -band photometric brightness temperatures and compare these to *Spitzer* brightness temperatures. We also consider how this trend compares to inferences of thermal (non-)inversions from retrievals in the literature.

WASP-43b and HD 209458b are ideal cases to demonstrate the trend found in our models as they have water detections (Kreidberg et al. 2014; Line et al. 2016), suggesting an oxygen-rich composition. Both planets have also been found not to host thermal inversions using retrieval techniques (Blecic et al. 2014; Diamond-Lowe et al. 2014; Kreidberg et al. 2014; Stevenson et al. 2014; Line et al. 2016). Therefore, we expect both planets to have  $T_{4.5\mu m} < T_{3.6\mu m} < T_J$  as described above. Indeed, Fig. 11 shows that this is the case. The *HST*/WFC3 brightness temperatures in the  $J$  band are consistent with or hotter than that for IRAC 1 (within error bars), and both are higher than the IRAC 2 brightness temperature. WASP-

18b shows the opposite trend,  $T_J < T_{3.6\mu m} < T_{4.5\mu m}$ , which would suggest a thermal inversion and indeed agrees with the inference of a thermal inversion by Sheppard et al. (2017). WASP-103b also has an inferred thermal inversion (Kreidberg et al. 2018). The brightness temperatures shown in Fig. 11 are inconclusive as the errorbars on the *Spitzer* brightness temperatures are quite large, though note that Kreidberg et al. (2018) reduce the *Spitzer* data differently to Garhart et al. (2020).

In contrast, WASP-121b, WASP-12b, and WASP-33b show evidence for different chemistries/disequilibrium processes to our models. WASP-121b has been inferred to host a thermal inversion (Evans et al. 2017), but it has a high  $J$ -band brightness temperature relative to IRAC 1 and IRAC 2, which are consistent within the errorbars. Furthermore, for WASP-12b the  $J$ -band and IRAC 2 brightness temperatures are significantly lower than that for IRAC 1. In the case of WASP-33b, the opposite is true: The  $J$ -band and IRAC 2 brightness temperatures are both significantly higher than that for IRAC 1. Thus, all three planets show a different brightness temperature trend compared to our oxygen-rich models. This could be due to chemical species that we have not considered here (e.g. FeH and TiH), other chemical disequilibrium mechanisms, a C/O ratio greater than 1, or offsets between instruments that are not considered here. Ultimately, while photometric metrics for assessing temperature gradients provide a useful initial assessment, their dependence on chemistry and the inherent complexity of planetary atmospheres is such that atmospheric retrievals are needed

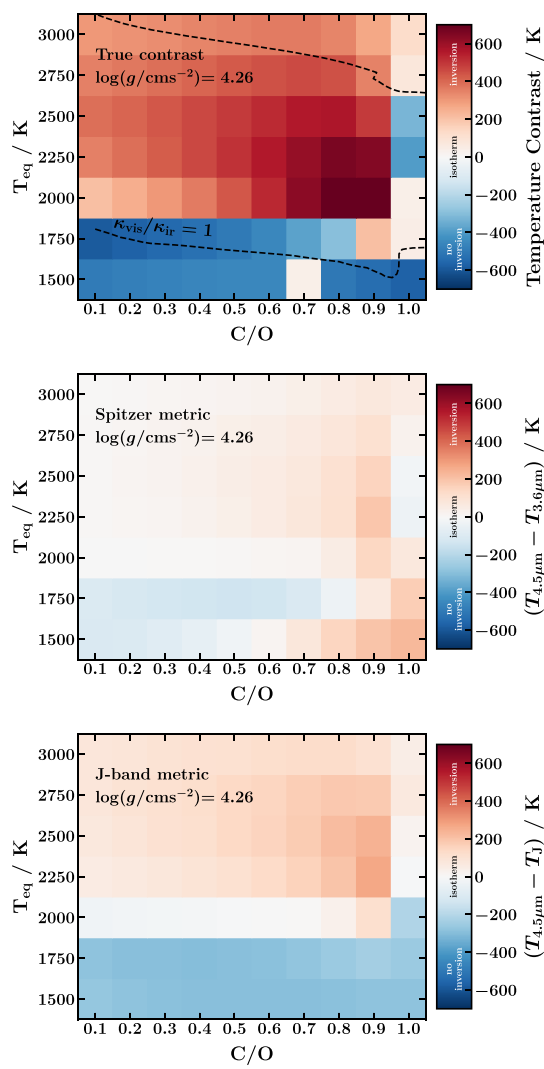


**Figure 10.** Same as centre column of Fig. 8 but for a planet with a higher gravity [ $\log(g/\text{cm}^{-2}) = 4.26$ , similar to WASP-18b, compared to  $\log(g/\text{cm}^{-2}) = 2.99$  in Fig. 8].

to confidently assess the presence of a thermal inversion or lack thereof.

Another use for comparing brightness temperatures for observed spectra is to provide a quick and empirical lower limit on the photospheric temperature gradient in the atmosphere. The larger the contrast between the maximum and minimum measured brightness temperatures, and the more precise they are, the stronger the constraints that can be placed on the photospheric temperature contrast. In particular, *HST*/WFC3 data can significantly improve the temperature contrasts determined with IRAC 1 and IRAC 2 data alone. For example, in the case of WASP-121b, the brightness temperature contrast based on the IRAC 1 and IRAC 2 measurements alone is  $70 \text{ K} \pm 100 \text{ K}$ , which is consistent with an isotherm. However, the range of brightness temperatures probed by the *HST*/WFC3 data is wider than that for the *Spitzer* data, and results in a temperature contrast of  $380 \text{ K} \pm 70 \text{ K}$ . Similarly, for WASP-33b, WASP-12b, and WASP-18b, the *HST*/WFC3 data also make significant improvements to the brightness temperature contrast. Note that uncertainty in the host star temperature can affect the errors in these brightness temperatures. In the cases shown here, we find that the largest error contributions from the stellar temperature are comparable to

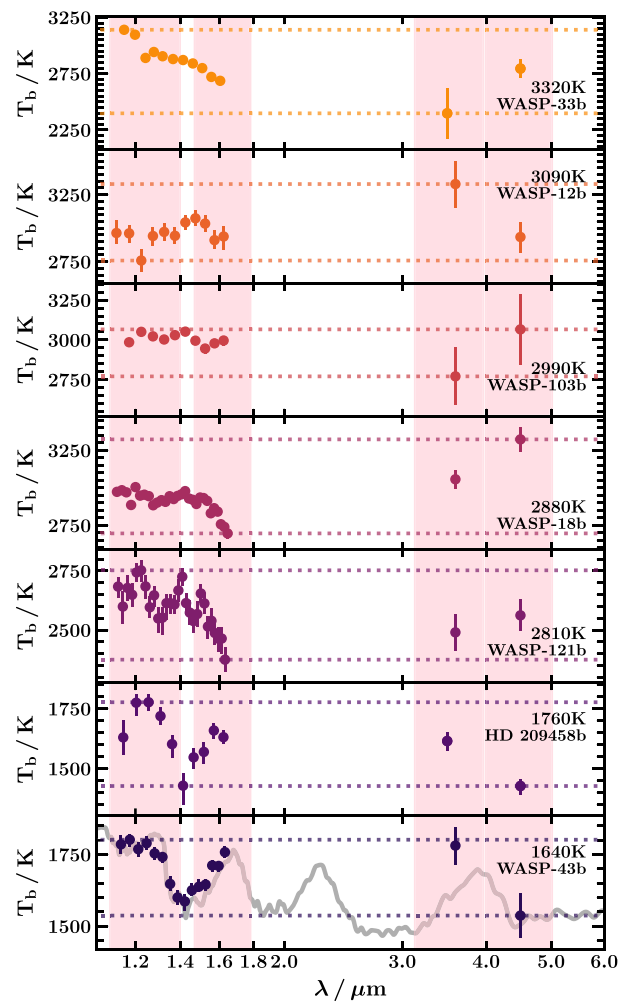


**Figure 11.** Brightness temperatures probed by *HST*/WFC3 and *Spitzer* IRAC 1 and IRAC 2 data for seven planets, ordered by equilibrium temperature. Nominal equilibrium temperatures are calculated assuming dayside-only redistribution and are labelled for each planet. The bottom panel shows the spectrum from Fig. 6 that corresponds to a non-inverted  $P$ - $T$  profile, for reference. *Spitzer* brightness temperatures for WASP-33b and HD 209458b are calculated using data from Deming et al. (2012) and Diamond-Lowe et al. (2014), respectively. Other *Spitzer* temperatures are from Garhart et al. (2020). *HST* brightness temperatures are calculated using spectra from Haynes et al. (2015) (WASP-33b), Kreidberg et al. (2014) (WASP-43b), Evans et al. (2017) (WASP-121b), Sheppard et al. (2017) (WASP-18b), Kreidberg et al. (2018) (WASP-103b), Stevenson et al. (2014) (WASP-12b), and Line et al. (2016) (HD 209458b). WASP-33b, WASP-18b, WASP-103b, and WASP-121b are reported to have thermal inversions in the literature while WASP-12b, WASP-43b, and HD 209458b have non-inverted profiles (see the references above). Planetary and stellar properties used to calculate the brightness temperatures are from Collier Cameron et al. (2010), Collins, Kielkopf & Stassun (2017), Gillon et al. (2012, 2014), Hellier et al. (2009, 2011), Southworth (2010, 2012), Delrez et al. (2016), and Stassun et al. (2017).

those from the flux uncertainties alone (i.e. the errorbars shown in Fig. 11) and therefore do not impact our assessment significantly. However, this effect should be treated rigorously for more detailed studies.

One of the reasons that the *HST*/WFC3 data help to place tighter constraints on some brightness temperature contrasts is that the signal-to-noise of the data is very good and results in tight

constraints on brightness temperature. This is despite the fact that, as shown by the blackbody curves in Fig. 6, a greater precision in flux is needed at shorter wavelengths for the same precision in brightness temperature. As a result, fairly precise spectral/photometric measurements are needed at shorter wavelengths in order to place tight constraints on brightness temperature. However, since the precision available with *HST/WFC3* allows excellent brightness temperature precision (reaching  $\sim 10$  K for some cases in Fig. 11), this effect does not preclude shorter wavelengths from this type of analysis. When using observations from other instruments, however, it is important to consider how the uncertainties in the fluxes will correspond to uncertainty in brightness temperature, which will depend on the wavelength range of the observations.

While we have used examples with the *HST/WFC3* and *Spitzer* data here, this analysis can also be performed with other observations and at different wavelengths. It is important to note that when comparing brightness temperatures from different instruments (including the analysis above), systematic offsets between the instruments can bias the temperature contrast obtained. One way to test for and characterize such offsets is by performing an atmospheric retrieval that includes a freely varying ‘offset’ parameter, which can then be retrieved from the data. Furthermore, future instruments such as the *James Webb Space Telescope’s* (*JWST*) NIRSpec will have much larger spectral ranges, allowing brightness temperatures to be measured across a wide range of wavelengths with the same instrument.

## 6 SUMMARY AND DISCUSSION

In this work, we investigate the importance of TiO in the spectral appearance and temperature structures of hot Jupiter atmospheres. To this end, we first examine the importance of the accuracy of TiO line lists for determining its observable spectral signatures in transmission and emission spectra, both at low and high resolutions. We further investigate the effect of TiO on the temperature structure of an atmosphere. To do this, we investigate the strength of thermal inversions as a function of C/O ratio, equilibrium temperature, metallicity, stellar type, and gravity, considering TiO as the inversion-causing molecule. In addition, we assess the performance of temperature gradient metrics as a function of these parameters.

We begin by comparing the recent TOTO TiO line list (McKemmish et al. 2019) to those of Schwenke (1998) and Plez 2012 (sourced from Ryabchikova et al. 2015) (hereafter, S98 and P12 line lists, respectively), focusing on the consequences for the interpretation of transmission, emission, and high-resolution Doppler spectra. Interpretation of high-resolution Doppler spectra using cross-correlation methods relies on accurate line positions and sufficiently strong planetary spectral features. We assess the accuracy of line positions in the TOTO line list by considering the fraction of energy levels and transitions that are taken from experimental data. For example, at 2000 K, there are 4491 transitions with line intensities above  $10^{-17}$  cm/molecule, of which 83 per cent are from experimental data and have high accuracy. Furthermore, experimental data for the  $v = 2$  and higher vibrational excitations of the B  $^3\Pi$  state are needed to fill in the strong spectral bands that are currently calculated theoretically.

For both transmission and emission spectra, we find that the differences between the TOTO and S98 line lists have the greatest impact on model spectra in the optical range. As a result, optical transmission spectra are strongly affected and the spectra generated with each line list can differ significantly depending on the spectral

resolution (almost 1000 ppm at  $R \sim 10^4$ ). Since thermal emission spectra of exoplanets are largely observed in the infrared spectral range, the differences between the TOTO and S98 line lists have a more subtle effect. For two model spectra generated with the same  $P-T$  profile but using each of the TiO line lists, the differences are only observable at higher resolutions (e.g. up to  $\sim 100$  ppm at a resolution of  $R \sim 10^4$  in the near-infrared).

Beyond the effects of TiO line lists, we also explore how TiO equilibrium chemistry can shape the thermal profile of an atmosphere. We investigate the equilibrium abundances of chemical species (calculated using the HSC CHEMISTRY software package) as a function of equilibrium temperature,  $T_{\text{eq}}$ , C/O ratio, metallicity, stellar host type, and planetary surface gravity. In turn, this allows an exploration of thermal inversions in this parameter space. Through semi-analytic considerations of radiative equilibrium, we find that thermal inversions can occur at the coolest equilibrium temperature for a C/O ratio of  $\sim 0.9$ , consistent with previous studies (e.g. Mollière et al. 2015; Gandhi & Madhusudhan 2019).

We further calculate self-consistent 1D model atmospheres and their spectra for a range of C/O ratios  $T_{\text{eq}}$ , metallicities, stellar types, and gravities. We include the effects of vertical mixing, as well as the variation of the energy redistribution factor as a function of  $T_{\text{eq}}$ . These models confirm the trend found by our simple analysis by which thermal inversions happen at cooler  $T_{\text{eq}}$  at C/O  $\approx 0.9$ . Furthermore, the transition from non-inverted to inverted  $P-T$  profiles happens at the expected temperature range of  $\sim 1750$ – $2000$  K for models with solar-like composition, where TiO is known to condense. We also find that for higher metallicity models, a higher equilibrium temperature is needed to cause a thermal inversion. Conversely, a later stellar type can result in thermal inversions occurring at cooler  $T_{\text{eq}}$ . We find that gravity has a smaller effect on thermal inversion strength compared to other parameters.

In order to characterize the strength of the inversions/non-inversions in our models, we assess a range of metrics based on the contrast in brightness temperature between two photometric bands. Although the brightness temperature contrast between *Spitzer*’s IRAC 1 and IRAC 2 channels is commonly used as an indication of inversion strength (e.g. Burrows et al. 2007; Knutson et al. 2010; Madhusudhan & Seager 2010), we find that in the case of H<sub>2</sub>O-dominated spectra a stronger temperature contrast can be observed by comparing the IRAC 2 channel to the *H* band or *J* band. Furthermore, we find that for high C/O ratios and low equilibrium temperatures, the IRAC 1 band contains significant opacity from CH<sub>4</sub> and HCN and, as such, does not provide a good measure of the spectral continuum. In this regime, an atmosphere without a thermal inversion can have a larger IRAC 2 flux compared to the IRAC 1 flux, mimicking the signature of a thermal inversion for lower C/O ratios. Similarly, the *J* band incorrectly infers a non-inversion at some C/O ratios for  $T_{\text{eq}} \sim 1750$  K, for example with a later stellar host type. Therefore, neither metric works optimally across the whole parameter space considered. We investigate this for observed spectra by finding the brightness temperature contrasts between the WFC3 and *Spitzer* IRAC 1 and IRAC 2 bands for various planets. While our oxygen-rich models show the trend that the *J* band is a clearer continuum band than the IRAC 1 band, several of these planets do not follow the same pattern. This is likely due to differences in chemistry and/or disequilibrium effects not considered in our models. Overall, we suggest that continuum opacity bands depend on the atmospheric chemistry and that temperature gradient metrics should therefore be used with caution as a single metric does not necessarily apply to all atmospheric chemistries.

Thermal inversions and the role of TiO in producing them remain a key part in understanding exoplanet atmospheres and the processes that shape them. As exoplanetary atmospheric observations continue to improve, it will be necessary to use the highest quality chemical cross-sections and understand the role of the many parameters that dictate the structure of an atmosphere in order to demystify these exotic worlds.

## ACKNOWLEDGEMENTS

AAAP thanks John Harrison for help with using HSC CHEMISTRY, and acknowledges financial support from the Science and Technology Facilities Council (STFC), UK, towards her doctoral programme. SG acknowledges support from the UK STFC research grant ST/S000631/1. We thank the anonymous reviewer for their very helpful comments on our manuscript.

## REFERENCES

- Arcangeli J. et al., 2018, *ApJ*, 855, L30  
 Barber R. J., Strange J. K., Hill C., Polyansky O. L., Mellau G. C., Yurchenko S. N., Tennyson J., 2014, *MNRAS*, 437, 1828  
 Beatty T. G., Madhusudhan N., Pogge R., Chung S. M., Bierlya A., Gaudi B. S., Latham D. W., 2017a, *AJ*, 154, 242  
 Beatty T. G., Madhusudhan N., Tsiaras A., Zhao M., Gilliland R. L., Knutson H. A., Shporer A., Wright J. T., 2017b, *AJ*, 154, 158  
 Bell K. L., Berrington K. A., 1987, *J. Phys. B At. Mol. Phys.*, 20, 801  
 Birkby J. L., 2018, Spectroscopic Direct Detection of Exoplanets. Springer Int. Publ., Cham, p. 1485  
 Blecic J. et al., 2014, *ApJ*, 781, 116  
 Bond J. C., Lauretta D. S., O'Brien D. P., 2010, *Icarus*, 205, 321  
 Brogi M., Snellen I. A. G., de Kok R. J., Albrecht S., Birkby J., de Mooij E. J. W., 2012, *Nature*, 486, 502  
 Burrows A., Volobuyev M., 2003, *ApJ*, 583, 985  
 Burrows A., Sudarsky D., Hubeny I., 2006, *ApJ*, 650, 1140  
 Burrows A., Hubeny I., Budaj J., Knutson H. A., Charbonneau D., 2007, *ApJ*, 668, L171  
 Burrows A., Iguel L., Hubeny I., 2008, *ApJ*, 682, 1277  
 Cartier K. M. S. et al., 2017, *AJ*, 153, 34  
 Castelli F., Kurucz R. L., 2003, in Piskunov N., Weiss W. W., Gray D. F., eds, Proc. IAU Symp. 210, Modelling of Stellar Atmospheres. Kluwer, Dordrecht, p. A20  
 Collier Cameron A. et al., 2010, *MNRAS*, 407, 507  
 Collins K. A., Kielkopf J. F., Stassun K. G., 2017, *AJ*, 153, 78  
 Cowan N. B., Agol E., 2011, *ApJ*, 729, 54  
 Crossfield I. J. M., Barman T., Hansen B. M. S., Tanaka I., Kodama T., 2012, *ApJ*, 760, 140  
 Császár A. G., Czakó G., Furtenbacher T., Mátyus E., 2007, *Annu. Rep. Comput. Chem.*, 3, 155  
 de Kok R. J., Birkby J., Brogi M., Schwarz H., Albrecht S., de Mooij E. J. W., Snellen I. A. G., 2014, *A&A*, 561, A150  
 Delrez L. et al., 2016, *MNRAS*, 458, 4025  
 Delrez L. et al., 2018, *MNRAS*, 474, 2334  
 Deming D. et al., 2012, *ApJ*, 754, 106  
 Diamond-Lowe H., Stevenson K. B., Bean J. L., Line M. R., Fortney J. J., 2014, *ApJ*, 796, 66  
 Elser S., Meyer M. R., Moore B., 2012, *Icarus*, 221, 859  
 Espinoza N. et al., 2019, *MNRAS*, 482, 2065  
 Evans T. M. et al., 2017, *Nature*, 548, 58  
 Fortney J. J., Cooper C. S., Showman A. P., Marley M. S., Freedman R. S., 2006, *ApJ*, 652, 746  
 Fortney J. J., Lodders K., Marley M. S., Freedman R. S., 2008, *ApJ*, 678, 1419  
 Furtenbacher T., Császár A. G., 2012, *J. Quant. Spectrosc. Radiat. Transfer*, 113, 929  
 Furtenbacher T., Császár A. G., Tennyson J., 2007, *J. Mol. Spectrosc.*, 245, 115  
 Gandhi S., Madhusudhan N., 2017, *MNRAS*, 472, 2334  
 Gandhi S., Madhusudhan N., 2019, *MNRAS*, 485, 5817  
 Gandhi S., Madhusudhan N., Mandell A., 2020, *AJ*, 159, 232  
 Garhart E. et al., 2020, *AJ*, 159, 137  
 Gillon M. et al., 2012, *A&A*, 542, A4  
 Gillon M. et al., 2014, *A&A*, 562, L3  
 Gordon I. E. et al., 2017, *J. Quant. Spectrosc. Radiat. Transfer*, 203, 3  
 Guillot T., 2010, *A&A*, 520, A27  
 Hansen B. M. S., 2008, *ApJS*, 179, 484  
 Harris G. J., Tennyson J., Kaminsky B. M., Pavlenko Y. V., Jones H. R. A., 2006, *MNRAS*, 367, 400  
 Harrison J. H. D., Bonsor A., Madhusudhan N., 2018, *MNRAS*, 479, 3814  
 Haynes K., Mandell A. M., Madhusudhan N., Deming D., Knutson H., 2015, *ApJ*, 806, 146  
 Hebb L. et al., 2009, *ApJ*, 693, 1920  
 Hellier C. et al., 2009, *Nature*, 460, 1098  
 Hellier C. et al., 2011, *A&A*, 535, L7  
 Hoeijmakers H. J., de Kok R. J., Snellen I. A. G., Brogi M., Birkby J. L., Schwarz H., 2015, *A&A*, 575, A20  
 Hubeny I., 2017, *MNRAS*, 469, 841  
 Hubeny I., Burrows A., Sudarsky D., 2003, *ApJ*, 594, 1011  
 John T. L., 1988, *A&A*, 193, 189  
 Knutson H. A., Charbonneau D., Allen L. E., Burrows A., Megeath S. T., 2008, *ApJ*, 673, 526  
 Knutson H. A., Charbonneau D., Burrows A., O'Donovan F. T., Mandushev G., 2009, *ApJ*, 691, 866  
 Knutson H. A., Howard A. W., Isaacson H., 2010, *ApJ*, 720, 1569  
 Kreidberg L. et al., 2014, *ApJ*, 793, L27  
 Kreidberg L. et al., 2018, *AJ*, 156, 17  
 Kurucz R. L., 1979, *ApJS*, 40, 1  
 Line M. R. et al., 2016, *AJ*, 152, 203  
 Lothringer J. D., Barman T., 2019, *ApJ*, 876, 69  
 Lothringer J. D., Barman T., Koskinen T., 2018, *ApJ*, 866, 27  
 Madhusudhan N., 2012, *ApJ*, 758, 36  
 Madhusudhan N., Seager S., 2010, *ApJ*, 725, 261  
 Madhusudhan N. et al., 2011a, *Nature*, 469, 64  
 Madhusudhan N., Mousis O., Johnson T. V., Lunine J. I., 2011b, *ApJ*, 743, 191  
 Mansfield M. et al., 2018, *AJ*, 156, 10  
 McKemmish L. K., Yurchenko S. N., Tennyson J., 2016, *MNRAS*, 463, 771  
 McKemmish L. K. et al., 2017, *ApJS*, 228, 15  
 McKemmish L. K., Masseron T., Hoeijmakers H. J., Perez-Mesa V., Grimm S. L., Yurchenko S. N., Tennyson J., 2019, *MNRAS*, 488, 2836  
 Menou K., 2012, *ApJ*, 754, L9  
 Mollière P., van Boekel R., Dullemond C., Henning T., Mordasini C., 2015, *ApJ*, 813, 47  
 Moriarty J., Madhusudhan N., Fischer D., 2014, *ApJ*, 787, 81  
 Moses J. I., Fouchet T., Bézard B., Gladstone G. R., Lellouch E., Feuchtgruber H., 2005, *J. Geophys. Res.: Planets*, 110, E08001  
 Moses J. I., Madhusudhan N., Visscher C., Freedman R. S., 2013, *ApJ*, 763, 25  
 Nugroho S. K., Kawahara H., Masuda K., Hirano T., Kotani T., Tajitsu A., 2017, *AJ*, 154, 221  
 Parmentier V., Showman A. P., Lian Y., 2013, *A&A*, 558, A91  
 Parmentier V. et al., 2018, *A&A*, 617, A110  
 Pasek M. A., Milson J. A., Ciesla F. J., Lauretta D. S., Sharp C. M., Lunine J. I., 2005, *Icarus*, 175, 1  
 Patrascu A. T., Yurchenko S. N., Tennyson J., 2015, *MNRAS*, 449, 3613  
 Pinhas A., Rackham B. V., Madhusudhan N., Apai D., 2018, *MNRAS*, 480, 5314  
 Plez B., 1998, *A&A*, 337, 495  
 Richard C. et al., 2012, *J. Quant. Spectrosc. Radiat. Transfer*, 113, 1276  
 Robinson T. D., Catling D. C., 2014, *Nat. Geosci.*, 7, 12  
 Rothman L. S. et al., 2010, *J. Quant. Spectrosc. Radiat. Transfer*, 111, 2139

- Rothman L. S. et al., 2013, *J. Quant. Spectrosc. Radiat. Transfer*, 130, 4  
 Ryabchikova T., Piskunov N., Kurucz R. L., Stempels H. C., Heiter U., Pakhomov Y., Barklem P. S., 2015, *Phys. Scr.*, 90, 054005  
 Schwenke D. W., 1998, *Faraday Discuss.*, 109, 321 (S98)  
 Seager S., Richardson L. J., Hansen B. M. S., Menou K., Cho J. Y. K., Deming D., 2005, *ApJ*, 632, 1122  
 Sedaghati E. et al., 2017, *Nature*, 549, 238  
 Sheppard K. B., Mandell A. M., Tamburo P., Gandhi S., Pinhas A., Madhusudhan N., Deming D., 2017, *ApJ*, 850, L32  
 Southworth J., 2010, *MNRAS*, 408, 1689  
 Southworth J., 2012, *MNRAS*, 426, 1291  
 Spiegel D. S., Silverio K., Burrows A., 2009, *ApJ*, 699, 1487  
 Stassun K. G., Collins K. A., Gaudi B. S., 2017, *AJ*, 153, 136  
 Stevenson K. B., 2016, *ApJ*, 817, L16  
 Stevenson K. B., Bean J. L., Madhusudhan N., Harrington J., 2014, *ApJ*, 791, 36  
 Swain M. et al., 2013, *Icarus*, 225, 432  
 Tennyson J. et al., 2016, *J. Mol. Spectrosc.*, 327, 73  
 Triaud A. H. M. J., 2014, *MNRAS*, 439, L61  
 Triaud A. H. M. J., Lanotte A. A., Smalley B., Gillon M., 2014, *MNRAS*, 444, 711  
 von Essen C., Mallonn M., Welbanks L., Madhusudhan N., Pinhas A., Bouy H., Weis Hansen P., 2019, *A&A*, 622, A71  
 Welbanks L., Madhusudhan N., 2019, *AJ*, 157, 206  
 White W. B., Johnson S. M., Dantzig G. B., 1958, *J. Chem. Phys.*, 28, 751  
 Yurchenko S. N., Tennyson J., 2014, *MNRAS*, 440, 1649  
 Yurchenko S. N., Barber R. J., Tennyson J., 2011, *MNRAS*, 413, 1828  
 Yurchenko S. N., Tennyson J., Barber R. J., Thiel W., 2013, *J. Mol. Spectrosc.*, 291, 69  
 Yurchenko S. N., Lodi L., Tennyson J., Stolyarov A. V., 2016, *Comput. Phys. Commun.*, 202, 262  
 Yurchenko S. N., Al-Refaie A. F., Tennyson J., 2018, *A&A*, 614, A131  
 Zahnle K., Marley M. S., Freedman R. S., Lodders K., Fortney J. J., 2009, *ApJ*, 701, L20

## APPENDIX A: EQUILIBRIUM CHEMISTRY CALCULATIONS

In the equilibrium chemistry calculations performed using the HSC CHEMISTRY software package, we use the species given in Bond et al. (2010) and Harrison et al. (2018) and include additional relevant species, as listed in Table A1. Although potassium and vanadium are not present in the equilibrium chemistry calculations, we include them in our atmospheric models by giving them the same vertical profiles as sodium and titanium, respectively, scaled according to the solar K/Na and V/Ti ratios, respectively.

**Table A1.** Species added to the HSC CHEMISTRY equilibrium chemistry calculations, on top of those used in Bond et al. (2010) and Harrison et al. (2018). All species listed here are in the gas phase.

Element	Species added
H	$H^-$ , $H^+$ , $H_2^-$ , $H_2^+$ , $H_3^+$ , $H_3$ , $(H_3)_2$ , $H(H_3)$
O	$O^-$ , $O^+$ , $O^{-2}$ , $O_2^-$ , $O_2^+$ , $O_2^{-2}$ , $O_3$
C	$C^-$ , $C^+$ , $C_2^-$ , $C_2^+$ , $C_2$ , $C_3$ , $C_4$ , $C_5$ , $C_6$ , $C_7$ , $C_8$ , $C_{60}$ , $C_{70}$
N	$N^-$ , $N^+$ , $N_2^-$ , $N_2^+$ , $N_3^-$ , $N_3$
Ti	$Ti^-$ , $Ti^+$ , $Ti^3+$ , $Ti_2$
Na	$Na$ , $Na^-$ , $Na^+$ , $Na_2$
Other	$OH$ , $OH^-$ , $OH^+$ , $C_2H_2$ , $C_2H_4$ , $e^-$

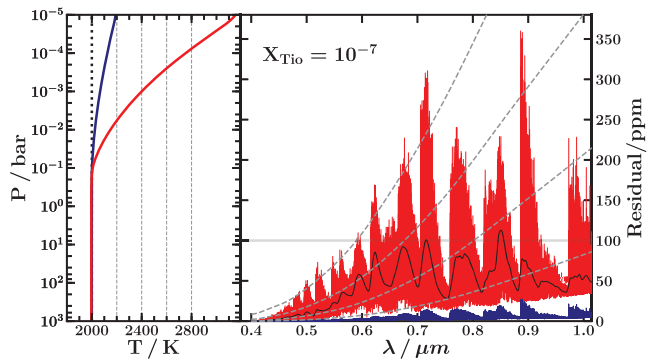


**Figure B1.** Line strengths of high-resolution ( $R \sim 10^5$ ) spectra compared to a blackbody spectrum for different temperature gradients. Residuals are calculated as the planet-star flux ratio of the atmosphere in question minus the planet-star flux ratio of an atmosphere whose  $P-T$  profile is a 2000 K isotherm (dashed black line in the left-hand panel). Right-hand panel: red and blue residuals correspond to the red and blue  $P-T$  profiles in the left-hand panel, respectively. The dashed grey lines correspond to isothermal  $P-T$  profiles at 2200, 2400, 2600, and 2800 K, respectively (shown by dashed grey lines in the left-hand panel). The solid back line is the residual for the same spectra as the red line, but with both spectra smoothed by a Gaussian of width 2.3 nm (similar to the PSF of *HST/WFC3*) to show representative line strengths for low-resolution spectra. The 100 ppm level is shown by the solid light grey line. These models only include opacity from  $TiO$  and CIA to highlight the  $TiO$  spectral lines. A constant-with-depth  $TiO$  mixing ratio of  $10^{-7}$  is used.

## APPENDIX B: EFFECT OF TEMPERATURE GRADIENT ON HIGH-RESOLUTION SPECTRA

Beyond line position accuracy, detecting a chemical signature from high-resolution Doppler spectra with cross-correlation methods also requires the planetary spectral features to be sufficiently strong. A significant factor in determining the strength of features in a spectrum is the atmospheric temperature gradient; a steeper temperature slope results in stronger absorption or emission lines (depending on the direction of the gradient).

Here, we consider the effect of the temperature gradient on line strength in high-resolution spectra. Fig. B1 shows high-resolution spectra for two different temperature gradients relative to an isotherm (the red and blue lines correspond to the steep and shallow temperature gradients, respectively). It is clear that the steeper temperature gradient results in significantly stronger features. This suggests that chemical signatures are acutely sensitive to the temperature gradient, especially at high resolution. For example, a 400 K temperature difference at 1 mbar can cause differences in the spectrum of up to 200 ppm, which may be observable. Conversely, the absence of any detectable chemical signatures in a high-resolution Doppler spectrum could be the result of a  $P-T$  profile that is very close to isothermal. Although this is also true of low-resolution spectra, high-resolution spectra are more sensitive to temperature gradient and a lack of spectral features could potentially place a tighter constraint on this gradient compared to low-resolution spectra. This can be seen from Fig. B1; the solid black line in the right-hand panel shows the residual spectrum at lower resolution (to generate this, the spectra used to calculate the red line are smoothed by a Gaussian of width 2.3 nm before calculating the residual, to represent smoothing by the PSF of *HST/WFC3*). By comparing the high-resolution (red) and low-resolution (black) residuals, we see that the features are smoothed

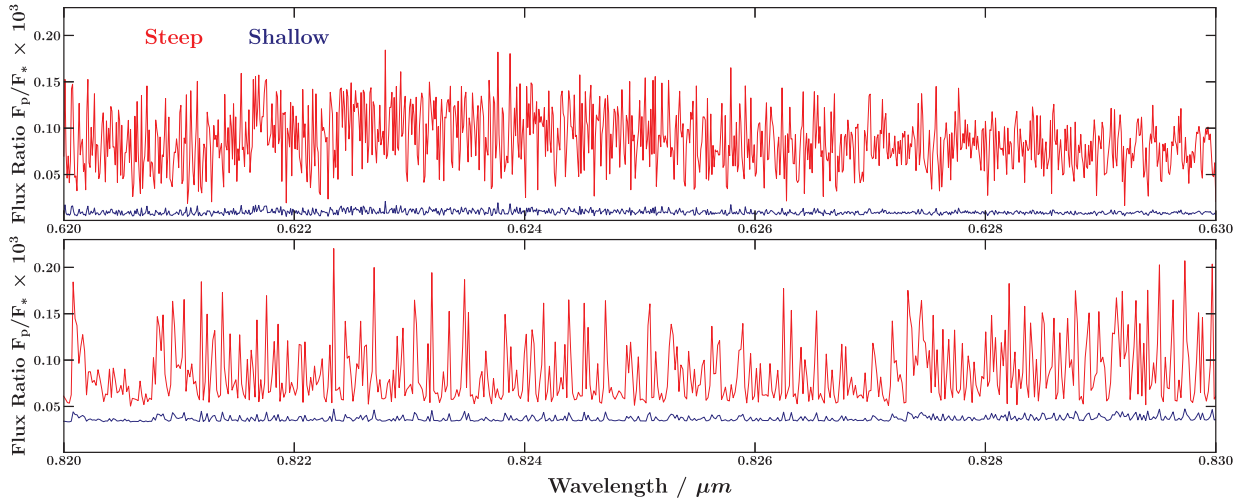


**Figure B2.** High-resolution ( $R \sim 10^5$ ) model spectra corresponding to a steep (red) and shallow (blue)  $P-T$  profile (steep and shallow  $P-T$  profiles are shown in the left-hand panel of Fig. B1 in red and blue, respectively). The spectra are calculated in the same way as in Fig. B1. Each panel spans  $0.01 \mu\text{m}$  in the range  $0.62-0.83 \mu\text{m}$  to give an overview of the differences in line strength between the two spectra in this range.

out and weakened at low resolution and, as such, high-resolution spectra are more sensitive to shallow temperature gradients given a fixed observation sensitivity. This effect can be seen in greater detail in Fig. B2, which shows a zoomed-in view of the high-resolution spectra corresponding to the blue and red  $P-T$  profiles from Fig. 6.

Fig. B1 also demonstrates that high-resolution spectra are sensitive to very low pressures in the atmosphere. The dashed grey lines in the right-hand panel correspond to isotherms at 2200, 2400, 2600, and 2800 K, and their crossing points with each residual spectrum indicate the temperatures probed by the spectrum at those wavelengths. For example, the strongest features in the red spectrum cross the spectrum corresponding to 2800 K, showing that this high-resolution spectrum is sensitive down to pressures of  $\sim 10^{-4}$  bar or lower (i.e. the pressure at which the temperature of the red  $P-T$  profile is 2800 K). Conversely, the low-resolution residual spectrum does not probe temperatures hotter than  $\sim 2600$  K, which corresponds to a pressure of  $\sim 3 \times 10^{-4}$  bar for this  $P-T$  profile, and does so with a significantly smaller signal.

### APPENDIX C: EFFECT OF METALLICITY ON EQUILIBRIUM CHEMISTRY

Fig. C1 shows the effect of metallicity on the equilibrium abundances of TiO, H<sub>2</sub>O, and CO as well as  $\kappa_{\text{vis}}/\kappa_{\text{ir}}$ . As expected, the abundances increase with metallicity. Furthermore, as metallicity increases, the partial pressure of TiO also increases and the temperatures at which TiO is depleted by condensation or thermal dissociation also increase. As a result,  $\kappa_{\text{vis}}/\kappa_{\text{ir}}$  peaks at higher temperature for higher metallicity.

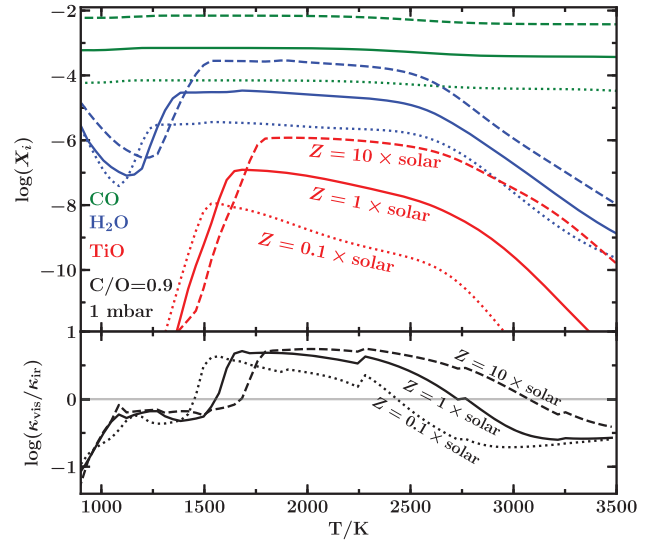


**Figure C1.** Top panel: abundances of TiO (red), H<sub>2</sub>O (blue), and CO (green) as a function of temperature for metallicities of 0.1, 1, and  $10 \times$  solar (dotted, solid, and dashed lines, respectively). Abundances are shown for a pressure of 1 mbar and a C/O ratio of 0.9. Lower panel:  $\kappa_{\text{vis}}/\kappa_{\text{ir}}$  for metallicities of 0.1, 1, and  $10 \times$  solar (dotted, solid, and dashed lines, respectively), also evaluated at 1 mbar and C/O = 0.9.

This paper has been typeset from a TeX/LaTeX file prepared by the author.